Precision analysis of the redshift-space galaxy bispectrum

Mikhail M. Ivanov,[1,*] Oliver H. E. Philcox,[1,2] Takahiro Nishimichi,[3,4] Marko Simonović,[5]
Masahiro Takada,[4] and Matias Zaldarriaga[1]

[1]*School of Natural Sciences, Institute for Advanced Study, 1 Einstein Drive, Princeton, New Jersey 08540, USA*
[2]*Department of Astrophysical Sciences, Princeton University, Princeton, New Jersey 08540, USA*
[3]*Center for Gravitational Physics, Yukawa Institute for Theoretical Physics, Kyoto University, Kyoto 606-8502, Japan*
[4]*Kavli Institute for the Physics and Mathematics of the Universe (WPI), UTIAS The University of Tokyo, Kashiwa, Chiba 277-8583, Japan*
[5]*Theoretical Physics Department, CERN, 1 Esplanade des Particules, Geneva 23 CH-1211, Switzerland*

(Received 19 October 2021; accepted 12 January 2022; published 10 March 2022)

We study the information content of the angle-averaged redshift space galaxy bispectrum. The main novelty of our approach is the use of a systematic tree-level perturbation theory model that includes galaxy bias, IR resummation, and also accounts for nonlinear redshift space distortions, binning, and projection effects. We analyze data from the perturbation theory challenge simulations, whose cumulative volume of 566 $h^{-3}\,\mathrm{Gpc}^3$ allows for a precise comparison to theoretical predictions. Fitting the power spectrum and bispectrum of our simulated data, and varying all necessary cosmological and nuisance parameters in a consistent Markov chain Monte Carlo analysis, we find that our tree-level bispectrum model is valid up to $k_{\mathrm{max}} = 0.08\ h\,\mathrm{Mpc}^{-1}$ (at $z = 0.61$). We also find that inclusion of the bispectrum monopole improves constraints on cosmological parameters by (5–15)% relative to the power spectrum. The improvement is more significant for the quadratic bias parameters of our simulated galaxies, which we also show to deviate from biases of the host dark matter halos at the $\sim 3\sigma$ level. Finally, we adjust the covariance and scale cuts to match the volume of the BOSS survey, and estimate that within the minimal ΛCDM model the bispectrum data can tighten the constraint on the mass fluctuation amplitude σ_8 by roughly 10%.

DOI: 10.1103/PhysRevD.105.063512

I. INTRODUCTION

The three-point function, or its Fourier transform the bispectrum [1], is the simplest statistic beyond the power spectrum that captures information about the large-scale spatial distribution of galaxies. The shape dependence of the bispectrum is sensitive to cosmological initial conditions, gravitational instability, and galaxy formation physics. For this reason the bispectrum is an important observational probe which can improve our understanding of both galaxy formation and fundamental cosmology [2,3]. It has been argued that it may help sharpen the limits on conventional cosmological parameters [3–6], neutrino masses [6–8], and primordial non-Gaussianity [4,9,10]. While these results are encouraging, they are often based on idealized Fisher forecasts and overoptimistic assumptions about the validity of theoretical models needed to describe the data. Most of the detailed comparisons of theoretical models to large-volume simulations and joint galaxy power spectrum and bispectrum fits were done in real space [11–13]. However, these works have ignored redshift space distortions, which are an important observational effect that breaks many degeneracies, but which are, at the same time, the largest source of nonlinearities. Therefore, it remains unclear whether the inclusion of the bispectrum really makes a difference in a realistic analysis of spectroscopic data, once all relevant cosmological and nuisance parameters are varied.

A quantitative answer to this question cannot be given without performing a consistent data analysis. While the three-point functions and bispectra of the galaxy density field have been measured both in simulations and in a number of past and current datasets (e.g. Zwicky and Lick catalogs [14,15], IRAS [16,17], WiggleZ [18], Baryon Oscillation Spectroscopic Survey (BOSS) [19–22]), the proper cosmological analyses of the bispectrum are still lacking. This is clearly in sharp contrast with the galaxy power spectrum analyses, which have been routinely used

---

[*] ivanov@ias.edu

as an important source of information on cosmological parameters. There are multiple factors that make the bispectrum analysis much more challenging.

From the computational side, the main challenge is a large number of data points, which correspond to triangle configurations formed by three wave vectors $\mathbf{k}_1$, $\mathbf{k}_2$, $\mathbf{k}_3$. Typical bispectra datasets consist of hundreds of triangles, which makes it hard to estimate the bispectrum from catalogs, compute the covariance matrix, and perform likelihood analysis. This stimulated the development of fast estimators [23–27], various compression techniques [2,28–30], and efficient mock catalog pipelines [31].

From the theory side, the main challenge is modeling nonlinear effects of matter clustering, galaxy bias, and redshift space distortions. Recent analyses described these effects by means of N-body simulations, which were used to calibrate phenomenological bispectrum models [19–21,32,33]. This simulation-based approach naturally extends to "emulation," in which the data is fitted directly to the simulation output [7,8,34–36]. Despite significant progress in numerical modeling of galaxy clustering over last years, it is not yet clear if emulators can meet precision requirements of future surveys, see e.g. [37]. The main issue is persistent uncertainty in galaxy formation physics, which has to be marginalized over in order to obtain robust cosmological constraints. This motivates the development of more conservative perturbative techniques [38–41], which have recently taken nonlinear large-scale structure modeling to a new precision level by virtue of the progress in the effective field theory (EFT) of large-scale structure [42,43].[1]

Unlike simulation-based approaches, EFT is fundamentally restricted to scales larger than $2\pi k_{\rm NL}^{-1} \sim 10$ Mpc. However, in the regime where it is applicable, EFT allows calculations to arbitrary order, and hence it provides a program of systematic successive approximations to the true answer. Moreover, by construction, EFT covers all possible galaxy formation scenarios by means of "nuisance parameters," which fully capture the impact of galaxy evolution on large scale clustering. Thus, this framework is naturally designed for the marginalization over galaxy formation physics, which boils down to a literal marginalization over nuisance parameters. Finally, EFT-based theoretical templates for a given cosmological model can be quickly generated with modifications of Boltzmann codes, e.g. [44–46], which allow one to efficiently explore the cosmology-dependence of large-scale structure data.

The full utility of the EFT approach has been shown recently in the analysis of the galaxy power spectrum data from BOSS [47]. This has resulted in first-ever measurements of *fundamental* cosmological parameters, such as the Hubble constant and the amplitude of the primordial scalar fluctuations, from the full shape of the galaxy power spectrum [48,49]. Moreover, the EFT-based full shape analyses have opened up a new opportunity to testing beyond-ΛCDM scenarios in a rigorous and self-consistent fashion [45,50–53].

An important step in applying the EFT calculations to the real data was the validation of the EFT-based power spectrum likelihoods on high-fidelity simulations [48,49,53,54]. In particular, the EFT-based pipelines have passed a blind test on galaxy mock catalogs called the "perturbation theory (PT) challenge" [55].[2] The PT challenge simulation suite covers a cumulative volume of 566 $h^{-3}\,\mathrm{Gpc}^3$, which is significantly larger than the volume of current and planned surveys. This large volume is chosen with the purpose of dramatically reducing statistical error and thereby identifying systematic uncertainties in theoretical modeling at the unprecedented subpercent level.

Inspired by the success of the EFT approach in the power spectrum analysis, in this work we extend the study of the PT challenge simulation data from Ref. [55] to the galaxy bispectrum. We analyze this data with the currently available tree-level EFT model.[3] The two main goals of our work are (1) to define the validity range of this model and to (2) assess the information content of the redshift-space galaxy bispectrum in the tree-level approximation. Achieving these goals will bring us one step closer to understanding the information content of the galaxy bispectrum and building a pipeline that can be used to analyze real data.

The paper is structured as follows. We describe the PT challenge simulations in Sec. II. Section III describes in detail our theoretical model. In Sec. IV we discuss our baseline power spectrum and bispectrum likelihoods. Our main results are presented in Sec. V, where we analyze the real space and redshift space monopole bispectrum data in combination with the baseline redshift space power spectrum likelihood. We discuss improvements in cosmological and bias parameters and give a forecast for a BOSS-like survey. There we also compare the measured values of galaxy bias parameters with those expected from dark matter halo relations. We compare our analysis with

---

[1] In what follows we will not distinguish between perturbation theory and the EFT, as the EFT is the only consistent realization of large-scale structure perturbation theory.

[2] The aim of this challenge is to test various methods of cosmological parameter inference from large-scale structure data in a blind way. The Reader is welcome to participate. The challenge details can be found at https://www2.yukawa.kyoto-u.ac.jp/takahiro.nishimichi/data/PTchallenge/.

[3] Perturbation theory one-loop bispectra of matter and halos in real space have been studied in Refs. [11–13,56–63]. While these calculations have not yet been extended to the realistic case of galaxy clustering in redshift space, certain relevant ingredients are already available in the literature, e.g. the redshift-space mapping in the EFT [64–66], the perturbative bias model [67–72], IR resummation to describe the nonlinear evolution of baryon acoustic oscillations [73,74], and grid-based calculations for the matter bispectrum [75].

previous works in Sec. VI and draw conclusions in Sec. VII. Several appendices contain additional material and tests. In Appendix A we validate our binning approach, and in Appendix B we show that "open" triangles do not carry any significant cosmological information. In Appendix C we test our covariance matrix choices. Our baseline power spectrum likelihood is described in Appendix D. Appendix E contains an analysis of the power spectrum and bispectrum purely in real space. Theoretical calculations of the power spectrum and bispectrum covariance matrices in perturbation theory are presented in Appendix F, while Appendix G contains a derivation of the Gaussian fingers-of-God damping.

II. DATA

The PT challenge simulation suite consists of 10 boxes, each with the side length $L = 3840\ h^{-1}\,\mathrm{Mpc}$. The gravitational evolution was traced by 3072^3 particles in each box. In this paper we consider one particular snapshot taken at $z = 0.61$, which corresponds to the BOSS CMASS1 sample [47]. The dark matter halos from this snapshot were populated with mock CMASS-like red luminous galaxies following the halo occupation distribution (HOD) prescription detailed in Ref. [55]. We refer the reader to this reference for further details on the simulations. The redshift-space power spectrum multipoles $\ell = 0, 2, 4$ were estimated as

$$\hat{P}_\ell(k_i) = \frac{2\ell+1}{N_i}\sum_{\tilde{\mathbf{k}}\in k_i}\mathcal{L}_\ell(\mu_{\tilde{\mathbf{k}}})\hat{P}(\tilde{\mathbf{k}}), \tag{2.1}$$

where we have introduced

$$\hat{P}(\tilde{\mathbf{k}}) = \frac{\tilde{V}|\delta_{\tilde{\mathbf{k}}}|^2 - \bar{n}^{-1}}{W^2_{\mathrm{CIC}}(\tilde{\mathbf{k}})}, \qquad \tilde{V} = \left(\frac{D_A^{(\mathrm{fid})}(z)}{D_A^{(\mathrm{true})}(z)}\right)^2 \frac{H^{(\mathrm{true})}(z)}{H^{(\mathrm{fid})}(z)} L^3, \tag{2.2}$$

and $\delta_{\tilde{\mathbf{k}}}$ is the Fourier space overdensity field, the sum runs over all modes whose norms belong to a bin $[(i-1)\Delta k, i\Delta k]$, we use $\Delta k = 0.01\ h\,\mathrm{Mpc}^{-1}$ and N_i is the number of Fourier modes in the bin. The modes in the sum in Eq. (2.1) are composed of fundamental modes $k_f = 2\pi L^{-1}$, which were rescaled by the Alcock-Paczynski (AP) effect [76] as

$$\tilde{k}_{f,x} = k_{f,x}\frac{D_A^{(\mathrm{true})}(z)}{D_A^{(\mathrm{fid})}(z)}, \qquad \tilde{k}_{f,y} = k_{f,y}\frac{D_A^{(\mathrm{true})}(z)}{D_A^{(\mathrm{fid})}(z)},$$
$$\tilde{k}_{f,z} = k_{f,z}\frac{H^{(\mathrm{fid})}(z)}{H^{(\mathrm{true})}(z)}, \tag{2.3}$$

where the upper scripts (true) and (fid) denote the comoving angular diameter distance $D_A(z)$ and the Hubble parameter $H(z)$ calculated in the true and fiducial cosmologies, respectively. The fiducial cosmological model is the same as in Ref. [55], flat ΛCDM with $\Omega_m^{(\mathrm{fid})} = 0.3$. Note that we have subtracted the Poissonian shot noise power spectrum contribution

$$\frac{1}{\bar{n}} = \frac{L^3}{N_{\mathrm{gal}}}, \tag{2.4}$$

where N_{gal} is the total number of galaxies, taking into account the interlacing technique for the aliasing correction and the cloud-in-a-cell (CIC) window function. If not stated otherwise, we will be using the data vector $[P_0, P_2, P_4]$ with $k_{\mathrm{max}} = 0.14\ h\,\mathrm{Mpc}^{-1}$. In addition, we employ the transverse moment Q_0 (equivalent of the real space power spectrum), which is estimated from the redshift space multipoles via

$$\hat{Q}_0 = \hat{P}_0 - \frac{1}{2}\hat{P}_2 + \frac{3}{8}\hat{P}_4, \tag{2.5}$$

see Refs. [77] for more detail and also Refs. [78–80] for earlier works. We use Q_0 in the range of scales

$$0.14\ h\,\mathrm{Mpc}^{-1} \leq k < 0.4\ h\,\mathrm{Mpc}^{-1},$$

so that it is not correlated with the multipoles' data vector.

The angle-averaged (monopole) bispectrum is computed using the following estimator:

$$\hat{B}_0(k_1,k_2,k_3) = \frac{1}{N_B(k_1,k_2,k_3)} \times \sum_{\tilde{\mathbf{q}}_1\in k_1}\sum_{\tilde{\mathbf{q}}_2\in k_2}\sum_{\tilde{\mathbf{q}}_3\in k_3}\delta_{\mathrm{K}}(\tilde{\mathbf{q}}_{123})\delta_{\tilde{\mathbf{q}}_1}\delta_{\tilde{\mathbf{q}}_2}\delta_{\tilde{\mathbf{q}}_3}, \tag{2.6}$$

where $\tilde{\mathbf{q}}_{123} \equiv \tilde{\mathbf{q}}_1 + \tilde{\mathbf{q}}_2 + \tilde{\mathbf{q}}_3$, and $\delta_{\mathrm{K}}(\mathbf{q}_{123})$ denotes the Kronecker delta function,

$$\delta_K(\mathbf{q}_{123}) = \begin{cases} 1, & \text{if } \mathbf{q}_{123} = 0 \\ 0, & \text{otherwise} \end{cases}, \tag{2.7}$$

and $N_B(k_1,k_2,k_3)$ is the number of fundamental triangles in the bin defined by wave number centers (k_1,k_2,k_3). Each bin has width $\Delta k = 0.01\ h\,\mathrm{Mpc}^{-1}$, which is the same as for the power spectrum estimator. We measure all nonequivalent bispectrum configurations with $k_1 \geq k_2 \geq k_3$. Note that unlike the power spectrum, we do not subtract the shot noise contributions from the bispectrum. As we show shortly, one of the shot noise corrections to the bispectrum depends on the deterministic power spectrum, i.e. it has the form $P_{\mathrm{lin}}\bar{n}^{-1}$. This carries cosmological information and therefore should not be subtracted. For consistency, we do not subtract the purely stochastic correction as well, although this choice is only a matter of convenience. The estimator Eq. (2.6) is evaluated with FFTs using the Scoccimarro method [23].

The real space bispectrum is calculated using the same formula Eq. (2.6), but with the real space density $\delta^{\rm real}_{\mathbf{k}}$ and without the AP effect.

III. THEORY MODEL

Let us describe our theoretical model for the redshift space bispectrum. We will discuss each relevant component separately.

In what follows we will work in the plane-parallel approximation. The galaxy density contrast field in redshift space at quadratic order in perturbation theory reads [66,72]

$$\begin{aligned}\delta^{(z)}(\mathbf{k}) = Z_1(\mathbf{k})\delta^{(1)}(\mathbf{k}) + [Z_2(\delta^{(1)})^2]_{\mathbf{k}} + d_1\epsilon(\mathbf{k}),\\ + d_2 b_1[\delta^{(1)}\epsilon]_{\mathbf{k}} - i f k_z d_1\left[\epsilon\frac{\hat z_i\partial_i}{\Delta}\theta^{(1)}\right]_{\mathbf{k}} + \cdots,\end{aligned} \tag{3.1}$$

where $[\ldots]_{\mathbf{k}}$ denotes a Fourier-space convolution, $\hat z_i$ is the line-of-sight direction unit vector, $\delta^{(1)}, \theta^{(1)}$ are linear matter density and velocity divergence fields (satisfying $\theta^{(1)} = \delta^{(1)}$); ϵ is the stochastic galaxy overdensity field, d_1, d_2 are free parameters, and the standard perturbation theory [81] kernels are given by

$$Z_1(\mathbf{k}) = b_1 + f\mu^2, \tag{3.2a}$$

$$\begin{aligned}Z_2(\mathbf{k}_1,\mathbf{k}_2) = {}&\frac{b_2}{2} + b_{\mathcal{G}_2}\left(\frac{(\mathbf{k}_1\cdot\mathbf{k}_2)^2}{k_1^2k_2^2} - 1\right)\\ &+ b_1F_2(\mathbf{k}_1,\mathbf{k}_2) + f\mu^2G_2(\mathbf{k}_1,\mathbf{k}_2)\\ &+ \frac{f\mu k}{2}\left(\frac{\mu_1}{k_1}(b_1+f\mu_2^2) + \frac{\mu_2}{k_2}(b_1+f\mu_1^2)\right),\end{aligned} \tag{3.2b}$$

$$F_2(\mathbf{k}_1,\mathbf{k}_2) = \frac{5}{7} + \frac{1}{2}\left(\frac{(\mathbf{k}_1\cdot\mathbf{k}_2)}{k_1^2} + \frac{(\mathbf{k}_1\cdot\mathbf{k}_2)}{k_2^2}\right) + \frac{2}{7}\frac{(\mathbf{k}_1\cdot\mathbf{k}_2)^2}{k_1^2k_2^2}, \tag{3.2c}$$

$$G_2(\mathbf{k}_1,\mathbf{k}_2) = \frac{3}{7} + \frac{1}{2}\left(\frac{(\mathbf{k}_1\cdot\mathbf{k}_2)}{k_1^2} + \frac{(\mathbf{k}_1\cdot\mathbf{k}_2)}{k_2^2}\right) + \frac{4}{7}\frac{(\mathbf{k}_1\cdot\mathbf{k}_2)^2}{k_1^2k_2^2}, \tag{3.2d}$$

where $\mu_i \equiv (\mathbf{k}_i\cdot\hat{\mathbf{z}})/k_i$, $\mu \equiv (\mathbf{k}\cdot\hat{\mathbf{z}})/k$, $\mathbf{k} \equiv \mathbf{k}_1 + \mathbf{k}_2$, and f is the logarithmic growth factor, related to the usual linear growth rate D_+ via

$$f = \frac{d\ln D_+}{d\ln a}, \tag{3.3}$$

with a being the scale factor in the Friedmann metric. The coefficients b_1, b_2, and $b_{\mathcal{G}_2}$ capture linear, quadratic, and tidal bias between matter and galaxies, respectively. The tree-level bispectrum is obtained by computing the three-point function of the perturbative density field at second order [71],

$$\begin{aligned}B_{\rm ggg}(\mathbf{k}_1,\mathbf{k}_2,\mathbf{k}_3) = {}&2Z_2(\mathbf{k}_1,\mathbf{k}_2)Z_1(\mathbf{k}_1)Z_1(\mathbf{k}_2)P_{\rm lin}(k_1)P_{\rm lin}(k_2)\\ &+ P_\epsilon(k_2)d_1(2d_2b_1 + d_1f\mu_1^2)Z_1(\mathbf{k}_1)P_{\rm lin}(k_1) + \text{cycl.} + d_1^3B_\epsilon(\mathbf{k}_1,\mathbf{k}_2,\mathbf{k}_3),\end{aligned} \tag{3.4}$$

where we have used the following correlation functions

$$\begin{aligned}\langle\delta^{(1)}(\mathbf{k})\delta^{(1)}(\mathbf{k}')\rangle &= (2\pi)^3\delta_D^{(3)}(\mathbf{k}+\mathbf{k}')P_{\rm lin}(k),\\ \langle\epsilon(\mathbf{k})\epsilon(\mathbf{k}')\rangle &= (2\pi)^3\delta_D^{(3)}(\mathbf{k}+\mathbf{k}')P_\epsilon(k),\\ \langle\epsilon(\mathbf{k}_1)\epsilon(\mathbf{k}_2)\epsilon(\mathbf{k}_3)\rangle &= (2\pi)^3\delta_D^{(3)}(\mathbf{k}_1+\mathbf{k}_2+\mathbf{k}_3)B_\epsilon(\mathbf{k}_1,\mathbf{k}_2,\mathbf{k}_3).\end{aligned} \tag{3.5}$$

A. Stochastic terms

At quadratic order in perturbation theory the shot-noise contributions are constants,

$$P_\epsilon = \text{const}, \qquad B_\epsilon = \text{const}. \tag{3.6}$$

Furthermore, if ϵ is Poisson distributed, both statistics are fully determined by the galaxy number density $\bar n$ (see e.g. Ref. [82] and references therein):

$$B_\epsilon = P_\epsilon^2 = \frac{1}{\bar n^2}. \tag{3.7}$$

However, due to halo exclusion, deviations from Poissonian sampling are known to be important [83–86], in which case we cannot use Eq. (3.7) and the tree-level bispectrum should be characterized by three free parameters capturing stochasticity. We define them to be $P_{\rm shot}$, $B_{\rm shot}$, and $A_{\rm shot}$:

$$\begin{aligned}&d_1^2\langle\epsilon^2\rangle = \frac{1+P_{\rm shot}}{\bar n}, \qquad d_1^3\langle\epsilon^3\rangle = \frac{A_{\rm shot}}{\bar n^2},\\ &B_{\rm shot} \equiv 2d_2d_1^{-1}(1+P_{\rm shot}),\end{aligned} \tag{3.8}$$

which are expected to be $\mathcal{O}(1)$ numbers. Importantly, the parameter $P_{\rm shot}$ also enters the power spectrum model. Furthermore, following [19,49,68] we will assume that the bispectrum and power spectrum of the stochastic overdensity component are correlated as in the Poissonian case (3.7), but their values are different from $\bar n^{-1}$, i.e.

$$B_\epsilon = P_\epsilon^2, \Rightarrow A_{\rm shot} = (1+P_{\rm shot})^2, \tag{3.9}$$

which is ultimately motivated by the expectation that departures from the Poissonian sampling are small. We have found that the bispectrum data is fully consistent with this hypothesis. Therefore, we adopt this choice as our baseline model for the stochastic nuisance parameters, which helps us reduce their number down to two.

B. Fingers-of-God effect

An important feature of nonlinear redshift-space distortions is the sensitivity to the stochastic velocity field, which can have relatively large scale correlations due to halo virialization [80]. This is called the "fingers-of-God" (FOG) effect [87]. In the EFT, FOG are captured perturbatively through the gradient expansion involving derivatives along the line of sight [46,64–66,88,89]. These corrections are called "counterterms," and at leading one-loop order they are given by [66]

$$\delta^{\rm ctr} = -c_0\left(\frac{k}{k_{\rm NL}}\right)^2 - (c_1\mu^2 + c_2\mu^4)\left(\frac{k}{k^r_{\rm NL}}\right)^2. \tag{3.10}$$

The role of μ-dependent counterterm coefficients c_1 and c_2 is to capture the physical impact of the FOG on large scale fluctuations.[4] In principle, the FOG is a one-loop effect in the EFT nomenclature, and it needs to be included along with other, "standard," one-loop corrections, which we ignore in this work. The characteristic momentum scale of these one-loop corrections matches the real space dark matter cutoff[5] $k_{\rm NL}$. If $2\pi/k^r_{\rm NL}$ is larger than $2\pi k_{\rm NL}^{-1}$ (and the cutoff of the bias expansion $2\pi k_{\rm M}^{-1}$), then the FOG counterterm can actually dominate over usual loop corrections. This is the exact situation that was observed for matter and galaxy power spectra in redshift space, where FOG corrections were found to be important even on relatively large scales where the "standard" loop corrections (i.e. without the counterterms) are suppressed [48,54,55,65,90].[6]

This motivates including the FOG counterterms c_1, c_2 in our theory model even though formally they capture one-loop effects, which we do not explicitly account for in our work. Another rationale behind this practice is that these counterterms can be treated as a proxy for the theoretical error [4,54]. Because of this reason, we do not assume any relationship between these parameters and those appearing in the redshift-space bispectrum model (see Appendix D for more detail). The additional bispectrum counterterms will also serve us as a tool to check if the tree-level calculation can be trusted: if the counterterm contribution dominates the tree-level bispectrum signal, the one-loop corrections cannot be ignored anymore.

In practice, we have found that it is sufficient to include only the $k^2\mu^2$ counterterm in our theory model. We ignore the contribution $k^2\mu^4$ because we have found that it is very degenerate with the $k^2\mu^2$ shape at the level of the bispectrum monopole, and hence we set $c_2 = 0$ in what follows. Note that we will have to include both c_1 and c_2 when we consider higher order angular multipole moments. The inclusion of the c_1 counterterm amounts to correcting the kernel Z_1 as

$$Z_1 \to Z_1^{\rm FOG} = b_1 + f\mu^2 - c_1\mu^2\left(\frac{k}{k^r_{\rm NL}}\right)^2. \tag{3.11}$$

In what follows we set $k^r_{\rm NL} = 0.3\ h\,{\rm Mpc}^{-1}$ in agreement with the measurement of the cutoff for the red luminous galaxies from the power spectrum of the PT challenge mocks [55,90].

C. IR resummation

Naïve attempts to build the EFT as a perturbative expansion in terms of smoothed (large-scale) density and velocity fields break down for the BAO part of the linear power spectrum (sometimes loosely referred to as the "BAO wiggles"). The procedure of resumming enhanced perturbative (loop) corrections to this part of the spectrum is called "IR resummation" [73,91–95] (see Refs. [96,97] for earlier works). IR resummation effects have to be included in the theory model even when it is evaluated at the tree level [73,92]. IR resummation for the bispectrum in redshift space has been calculated in Ref. [74] (see Ref. [98] for IR resummation of the bispectrum in the case of non-Gaussian initial conditions). At leading order this procedure amounts to the replacement of the linear matter power spectrum by its resummed version,

$$\begin{aligned} P_{\rm lin}(k) \to P^{\rm IR-res}_{\rm tree}(k) = {}& P_{\rm nw}(k) \\ & + P_{\rm w}(k){\rm e}^{-\Sigma^2k^2(1+f\mu^2(2+f)) - \delta\Sigma^2k^2f^2\mu^2(\mu^2-1)}, \end{aligned} \tag{3.12}$$

where $P_{\rm w}$ is the part of the spectrum that contains the BAO wiggles, $P_{\rm nw} \equiv P_{\rm lin} - P_{\rm w}$,

$$\begin{aligned} \Sigma^2 &= \frac{1}{6\pi^2}\int_0^{k_S} dq P_{\rm nw}(q)(1 - j_0(qr_{\rm BAO}) + 2j_2(qr_{\rm BAO})), \\ \delta\Sigma^2 &= \frac{1}{2\pi^2}\int_0^{k_S} dq P_{\rm nw}(q) j_2(qr_{\rm BAO}), \end{aligned} \tag{3.13}$$

---

[4] Strictly speaking, each coefficient c_i has "infinite" and "finite" pieces. The role of the infinite piece is to renormalize the UV part of one-loop integrals, whilst the "finite" part captures physical backreaction from short scales.

[5] The EFT calculations, at least at the one-loop order, can be interpreted as so-called standard perturbation theory [81] computations corrected with a set of UV "counterterms." In this picture the one-loop integrals have the same scaling for all tracers, while the tracer-specific momentum cutoffs appears only from the counterterms.

[6] Note that the form of the finite counterterms in Eq. (3.10) is quite similar to the large-scale limit of some phenomenological prescriptions for FOG, e.g. the Gaussian damping model, see Appendix G for more detail.

are the BAO damping functions, $j_\ell(x)$ are spherical Bessel functions, $r_{\rm BAO}$ is the comoving sound horizon at the drag epoch, k_S is the separation scale defining IR modes that need to be resummed. In practice we use $k_S = 0.05\ h/{\rm Mpc}$ following Ref. [73], although other choices, e.g. $k_S = k/2$ [92] give statistically indistinguishable results.

All in all, our final tree-level bispectrum model reads (cf. [72]):

$$
\begin{aligned}
B_{\rm ggg} =& [2Z_2(\mathbf{k}_1,\mathbf{k}_2)Z_1^{\rm FOG}(\mathbf{k}_1)Z_1^{\rm FOG}(\mathbf{k}_2)P_{\rm tree}^{\rm IR-res}(\mathbf{k}_1)P_{\rm tree}^{\rm IR-res}(\mathbf{k}_2)\\
&+\frac{1}{\bar n}(B_{\rm shot}b_1+(1+P_{\rm shot})f\mu^2)Z_1^{\rm FOG}(\mathbf{k}_1)P_{\rm tree}^{\rm IR-res}(\mathbf{k}_1)+{\rm cycl.}]+\frac{(1+P_{\rm shot})^2}{\bar n^2}, \qquad (3.14)
\end{aligned}
$$

where b_1, b_2, $b_{\mathcal{G}_2}$, $P_{\rm shot}$, $B_{\rm shot}$ are nuisance parameters to marginalize over. Note that $B_{\rm shot}$ is the only new parameter that is not present in the power spectrum model.

D. Redshift space multipoles

In real space the bispectrum depends on three kinematic variables (wavelengths) which characterize the shape of a triangle. In redshift space there appears an additional dependence due to the orientation of the triangle with respect to the line-of-sight direction. This orientation is characterized by two angles, which we choose, following Ref. [41], to be the polar angle of $\mathbf{k}_1$ [its cosine is $\cos\theta = \mu \equiv (\hat{\mathbf{k}}_1\cdot\hat{\mathbf{z}})$] and the azimuthal angle around $\mathbf{k}_1$ denoted by ϕ. In this case the angles between wave vectors $\mathbf{k}_a$ $(a = 1,2,3)$ and the line of sight are given by

$$
\begin{aligned}
&\mu_1 = \mu,\\
&\mu_2 = \mu\cos\alpha - (1-\mu^2)^{1/2}\sin\alpha\cos\phi,\\
&\mu_3 = -\frac{k_1}{k_3}\mu - \frac{k_2}{k_3}\mu_2, \qquad (3.15)
\end{aligned}
$$

where $\cos\alpha = x = (\hat{\mathbf{k}}_1\cdot\hat{\mathbf{k}}_2)$. It is convenient to describe this angular dependence by expanding $B_{\rm ggg}$ in spherical harmonics,

$$
\begin{aligned}
B_{\rm ggg}(\mathbf{k}_1,\mathbf{k}_2,\mathbf{k}_3) &= \sum_{\ell=0}^{\infty}\sum_{m=-\ell}^{\ell} B_{\ell m}(k_1,k_2,k_3)Y_{\ell m}(\theta,\phi),\\
B_{\ell m}(k_1,k_2,k_3) &= \frac{2\ell+1}{2}\int_0^{2\pi}d\phi\int_{-1}^{1}d(\cos\theta)\\
&\quad\times Y^*_{\ell m}(\theta,\phi)B_{\rm ggg}(\mathbf{k}_1,\mathbf{k}_2,\mathbf{k}_3). \qquad (3.16)
\end{aligned}
$$

In what follows we will focus on the $m = 0$ sector [23]. The corresponding momenta B_ℓ are called "bispectrum multipoles,"

$$
\begin{aligned}
B_\ell(k_1,k_2,k_3) &= \frac{2\ell+1}{2}\int_0^{2\pi}\frac{d\phi}{2\pi}\int_{-1}^{1}d(\cos\theta)\\
&\quad\times\mathcal{L}_\ell(\cos\theta)B_{\rm ggg}(\mathbf{k}_1,\mathbf{k}_2,\mathbf{k}_3), \qquad (3.17)
\end{aligned}
$$

where $\mathcal{L}_\ell$ denotes a Legendre polynomial of order ℓ. Note that the integral above can be done analytically at the tree level in the absence of IR resummation and the AP effect [41]. However, in what follows we will use the full formula (3.14) with IR resummation, and evaluate angular integrals in Eq. (3.17) numerically via Gauss-Legendre quadrature.

E. Alcock-Paczynski effect

The AP conversion [76] from true wave numbers and angles (q,ν) to observed wave numbers and angles (k,μ) is given by

$$
\begin{aligned}
&q^2 = k^2[\alpha_\parallel^{-2}\mu^2 + \alpha_\perp^{-2}(1-\mu^2)],\\
&\nu^2 = \alpha_\parallel^{-2}\mu^2[\alpha_\parallel^{-2}\mu^2 + \alpha_\perp^{-2}(1-\mu^2)]^{-1}, \qquad (3.18)
\end{aligned}
$$

which depends on the ratios between the true and fiducial Hubble parameters and angular diameter distances at the redshift of interest,

$$
\alpha_\parallel = \frac{H_{\rm fid}(z)}{H_{\rm true}(z)}\frac{H_{0,\rm true}}{H_{0,\rm fid}}, \quad \alpha_\perp = \frac{D_{\rm true,A}(z)}{D_{\rm fid,A}(z)}\frac{H_{0,\rm true}}{H_{0,\rm fid}}, \qquad (3.19)
$$

where additional factors $H_{0,\rm true}/H_{0,\rm fid}$ account for the fact that wave numbers are measured in $h{\rm Mpc}^{-1}$ units in our analysis. The observed power spectrum multipoles are given by [44]

$$
P_\ell(k) = \frac{2\ell+1}{2\alpha_\perp^2\alpha_\parallel}\int_{-1}^{1}d\mu\mathcal{L}_\ell(\mu)P_{\rm gg}(q[k,\mu],\nu[\mu]). \qquad (3.20)
$$

In full analogy, the bispectrum multipoles are given by [99]

$$
\begin{aligned}
&B_\ell(k_1,k_2,k_3)\\
&= \frac{2\ell+1}{2\alpha_\parallel^2\alpha_\perp^4}\int_0^{2\pi}\frac{d\phi}{2\pi}\int_{-1}^{1}d\mu_1\mathcal{L}_\ell(\mu_1)\\
&\quad\times B_{\rm ggg}(q_1[k_1,\mu_1],q_2[\ldots],q_3[\ldots],\nu_1[\mu_1],\nu_2[\mu_2(\mu_1)]), \qquad (3.21)
\end{aligned}
$$

where the observed angles satisfy Eq. (3.15). In what follows we will focus on the monopole moment $\ell = 0$, and leave the analysis of other multipoles for future work.

F. Binning effects

The measured bispectrum is a discrete approximation to a continuous Fourier-space field. In order to account for this discreteness we need to bin our theory predictions in the same way as we bin the data. Binning corrections are marginally important for the PT challenge power spectrum and it is straightforward to take them into account [55]. However, the situation is somewhat different for the bispectrum, where binning can be a serious source of systematics [100]. The exact discrete bispectrum that we extract from simulations is given by[7]

$$\hat{B}_{0,\mathrm{disc}}(k_1,k_2,k_3) = \frac{\sum_{\mathbf{q}_1\in k_1}\sum_{\mathbf{q}_2\in k_2}\sum_{\mathbf{q}_3\in k_3} B(\mathbf{q}_1,\mathbf{q}_2,\mathbf{q}_3)\delta_{\mathrm{K}}(\mathbf{q}_{123})}{N_B^{\mathrm{disc}}(k_1,k_2,k_3)},$$

$$N_B^{\mathrm{disc}}(k_1,k_2,k_3) = \sum_{\mathbf{q}_1\in k_1}\sum_{\mathbf{q}_2\in k_2}\sum_{\mathbf{q}_3\in k_3}\delta_{\mathrm{K}}(\mathbf{q}_{123}). \tag{3.22}$$

The sum in Eq. (3.22) runs over all discrete wave vectors $\mathbf{q}_i$ that belong to the triangle bin defined by its center (k_1,k_2,k_3) and width Δk. $N_B^{\mathrm{disc}}(k_1,k_2,k_3)$ is the total number of these "fundamental triangles" inside the triangle bin (k_1,k_2,k_3) [11].

Before going into technical details, let us outline our strategy. As a first step, we take the continuum limit, i.e. assume a vanishingly small fundamental wave number $k_f = (2\pi)L^{-1}$ as a leading approximation. In this first approximation the discreteness effects can be taken into account by integrating the continuous bispectrum field within appropriate bins. It is natural to refer to this program as the "integral approximation." Because the actual fundamental bin is finite, the integral approximation requires certain corrections. As a second step, we will introduce these corrections, which will be referred to as "discreteness weights."

Note that with our binning scheme there are so-called open triangle bins. The centers of these bins (k_1,k_2,k_3) do not satisfy momentum conservation constraints, such as $|k_3-k_2| < k_1 < k_3+k_2$.[8] In what follows we will discard these triangles because of three reasons:

(i) Their properties (and very existence) crucially depend on the box size, which makes it hard to make generic statements that would not depend on a particular survey volume.
(ii) The leading binning effect cannot be well captured by the integral approximation for these triangles, and hence it requires a significant modification of our baseline binning program.
(iii) These triangles do not carry any sizable cosmological information (at least at the level of the tree-level bispectrum likelihood) and with our particular choice of bins' width), see Appendix B.

As a first step of our binning procedure we implement the integral approximation. Other binning schemes were explored in Refs. [11,12,101]. The integral approximation amounts to replacing the sum over the modes with the Fourier integral,

$$\sum_{\mathbf{q}_1\in k_1}\sum_{\mathbf{q}_2\in k_2}\sum_{\mathbf{q}_1\in k_2}\delta_{\mathrm{K}}(\mathbf{q}_{123})B(\mathbf{q}_1,\mathbf{q}_2,\mathbf{q}_3) \to \frac{V^2}{(2\pi)^6}\int_{\mathbf{k}_1\mathbf{k}_2\mathbf{k}_3}(2\pi)^3\delta_D^{(3)}(\mathbf{q}_{123})B(\mathbf{q}_1,\mathbf{q}_2,\mathbf{q}_3),$$

$$\sum_{\mathbf{q}_1\in k_1}\sum_{\mathbf{q}_2\in k_2}\sum_{\mathbf{q}_1\in k_2}\delta_{\mathrm{K}}(\mathbf{q}_{123}) \to \frac{V^2}{(2\pi)^6}\int_{\mathbf{k}_1\mathbf{k}_2\mathbf{k}_3}(2\pi)^3\delta_D^{(3)}(\mathbf{q}_{123}), \tag{3.23}$$

where V is the box volume and we introduced

$$\int_{\mathbf{k}_1\mathbf{k}_2\mathbf{k}_3} \equiv \int_{V_{k_1k_2k_3}}\frac{d^3q_1}{(2\pi)^3}\frac{d^3q_2}{(2\pi)^3}\frac{d^3q_3}{(2\pi)^3}, \qquad V_{k_1k_2k_3} = \mathcal{D}_1\times\mathcal{D}_2\times\mathcal{D}_3,$$

$$\mathcal{D}_a = \left\{(q_{x_1},q_{x_2},q_{x_3})\in\mathbb{R}^3 : k_a - \frac{\Delta k}{2} \le |\mathbf{q}_a| \le k_a + \frac{\Delta k}{2}\right\}, \quad a = 1,2,3. \tag{3.24}$$

This way we arrive at

$$\hat{B}_{0,\mathrm{int}} = V^2\int_{\mathbf{k}_1\mathbf{k}_2\mathbf{k}_3}\frac{B(\mathbf{q}_1,\mathbf{q}_2,\mathbf{q}_3)}{N_{123}^T}(2\pi)^3\delta_D^{(3)}(\mathbf{q}_1+\mathbf{q}_2+\mathbf{q}_3),$$

$$N_{123} = V^2\int_{\mathbf{k}_1\mathbf{k}_2\mathbf{k}_3}(2\pi)^3\delta_D^{(3)}(\mathbf{q}_{123}) = 8\pi k_1k_2k_3\Delta k^3\frac{V^2}{(2\pi)^6}. \tag{3.25}$$

---

[7] We omit the subscript "ggg" for clarity in this section, i.e. replace $B_{\mathrm{ggg}} \to B$.

[8] Individual triangles that belong to the bin are, of course, valid triangles that satisfy all relevant constraints.

The delta function can be integrated explicitly following Ref. [102], yielding

$$\hat{B}_{0,\mathrm{int}} = \frac{V^2}{(2\pi)^6 N_{123}} \int_0^{2\pi} \frac{d\phi}{4\pi} \int_{-1}^{1} d\mu \left(\prod_{i=1}^{3} \int_{k_i-\Delta k/2}^{k_i+\Delta k/2} dq_i q_i \right) \quad B(q_1, q_2, q_3, \mu, \phi). \tag{3.26}$$

In order to estimate the accuracy of the integral approximation, we compare the continuous ($k_f \to 0$ limit) prediction for the number of triangle modes that fall in a given bin N_{123} with the actual number of discrete triangles in that bin N_B^{disc}. The result is shown in the upper left panel of Fig. 1, where we display the ratio $N_B^{\mathrm{disc}}/N_{123}$ for the bins whose centers satisfy the momentum conservation constraint, and which we actually use in the analysis. We see that the integral approximation correctly predicts the number of fundamental triangles for most of the bins, up to a few percent precision. However the integral approximation is not very accurate for folded triangles with $k_2 + k_3 = k_1 + \Delta k/2$. For these triangles the typical mismatch is about ~15%. This discrepancy also leads to a mismatch at the level of binned bispectra. To correct for this discrepancy we introduce "discreteness weights" w,

$$w = \frac{\hat{B}_{\mathrm{disc}}}{\hat{B}_{\mathrm{int}}}, \tag{3.27}$$

where $\hat{B}_{\mathrm{disc}}$ is computed by using a direct discrete expression Eq. (3.22), while $\hat{B}_{\mathrm{int}}$ is calculated from Eq. (3.25).

We compute the weights for a certain fiducial cosmology and nuisance parameters extracted from a fit to the simulation data analyzed without the weights. Since the evaluation of the full discrete expression Eq. (3.22) is too expensive for an Markov chain Monte Carlo (MCMC) method, the best strategy would be to iterate the discreteness weights for the best-fit bispectra from a few consecutive MCMC runs. However, quite remarkably, we have found that this iterative procedure has converged already at the first step. Our initial fiducial parameters happened to be

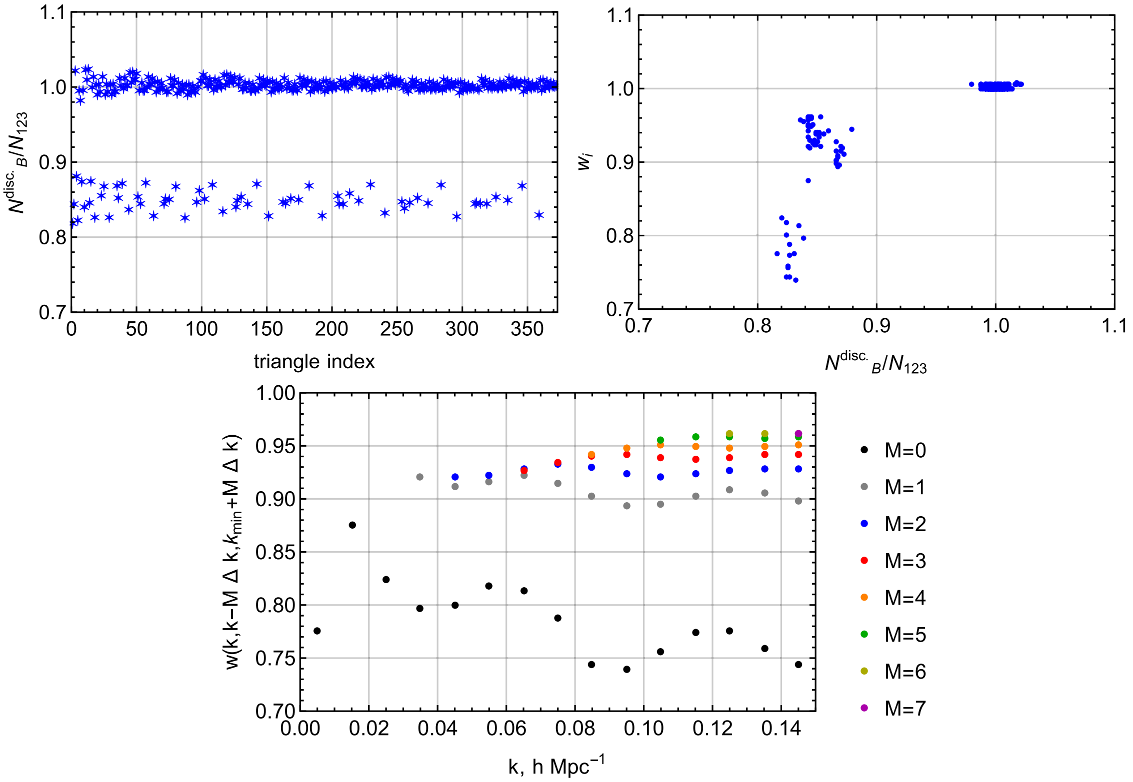

FIG. 1. Upper left panel: the ratio between the number of fundamental triangles from the data and from the integral approximation, $N_B^{\mathrm{disc}}/N_{123}$, as a function of the triangle bin. Upper right panel: the ratio between the exact binned bispectrum and the integral approximation ("discreteness weights" w_i), as a function of $N_B^{\mathrm{disc}}/N_{123}$ for the same triangle bins. The triangles shown correspond to $k_{\max} = 0.15\ h/\mathrm{Mpc}$. Lower panel: discreteness weights for folded triangles denoted by their bin centers (we use $\Delta k = 0.01\ h\,\mathrm{Mpc}^{-1}$, and hence $k_{\min} = \Delta k/2 = 5 \times 10^{-3}\ h\,\mathrm{Mpc}^{-1}$).

significantly different from the actual best-fit parameters, yet both produced almost identical discreteness weights. This shows that the discreteness weights are nearly cosmology independent, hence they can be computed only once for a given survey specification.

We display the discreteness weights for PT challenge boxes in the right panel of Fig. 1, along with the ratio $N_B^{\rm disc}/N_{123}$, which demonstrates that the "problematic" triangles can be easily identified in the data by comparing the number of fundamental triangles in the bin with the prediction of the integral approximation. As we can see from this figure, these corrections need to be included if $N_B^{\rm disc}/N_{123}$ deviates from unity by more than 10%. We show discreteness weights specifically for the problematic folded triangles in the lower panel of Fig. 1. For all other triangle configurations the discreteness weights coincide with unity with $\mathcal{O}(0.5)\%$ precision, implying that the integral approximation is very accurate for them.

Additionally, we validate our discreteness weights approach in Appendix A by comparing it with an approximate discrete binning scheme similar to Eq. (3.22). These tests suggest that our treatment of discreteness effects is accurate enough for the full simulation volume and hence can be safely adopted for the purposes of our paper and for any realistic future analysis.

All in all our theory model is given by

$$B^{\rm th} = \hat{B}_0^{\rm int}(k_1,k_2,k_3)w(k_1,k_2,k_3), \tag{3.28}$$

where $\hat{B}_0^{\rm int}$ is computed from Eq. (3.26) by numerically performing the five-dimensional integral over the tree-level IR resummed model (3.14).

IV. LIKELIHOOD

We will use a Gaussian likelihood for the bispectrum [3],

$$\ln \mathcal{L}_{\rm B} = -\frac{1}{2}\sum_{{\rm triangles}T'}(B_T^{\rm th}-B_T^{\rm data})(B_{T'}^{\rm th}-B_{T'}^{\rm data})(C^{\rm B})^{-1}_{TT'}, \tag{4.1}$$

where we assume without loss of generality that the bin centers satisfy $k_1 \geq k_2 \geq k_3$ and

$$\sum_T \equiv \sum_{k_1=k_{\rm min}}^{k_{\rm max}}\sum_{k_2=k_{\rm min}}^{k_1}\sum_{k_3=k_*}^{k_2}, \qquad k_* \equiv \max(k_{\rm min}, k_1-k_2). \tag{4.2}$$

The Gaussian likelihood approximation for the bispectrum is justified within perturbation theory, which is consistent with the tree-level approximation for the bispectrum itself. This approximation must be true on sufficiently large scales, to which we limit our analysis. In this regime we can use the Gaussian tree-level approximation for the covariance matrix $C^{\rm B}$ [3,23,41,99],

$$C^{\rm B}_{TT'} = \frac{(2\pi)^3\pi s_{123}}{k_1k_2k_3\Delta k^3 V_{\rm tot}}\delta_{TT'}\int_0^{2\pi}\frac{d\phi}{4\pi}\int_{-1}^{1}d\mu \times\prod_{i=1}^{3}\left[P_{\rm lin}(k_i)(b_1+f\mu_i^2(\phi,\mu))^2+\frac{1}{\bar{n}}\right], \tag{4.3}$$

where (k_1,k_2,k_3) denotes the center of the triangle bin T, $V_{\rm tot}$ is the cumulative volume of the PT challenge simulations ($V_{\rm tot} = 566\ h^{-3}\,{\rm Gpc}^3$), $s_{123} = 6$, 2, or 1 for equilateral, isosceles, and general triangles. To approximately account for the discreteness binning effects we use the true number of fundamental triangles in the bin instead of the prediction of the integral approximation, i.e. we rescale

$$C^{\rm B}_{TT'} \to \frac{N_{123}}{N_B^{\rm disc}}\cdot C^{\rm B}_{TT'}. \tag{4.4}$$

We evaluate the covariance for the best-fit cosmology extracted from the power spectrum likelihood analysis. We ignore the cross-covariance between the power spectrum and the bispectrum in our baseline analysis. This and other likelihood approximations are validated in Appendix C. There we show that our results are stable if we include the one-loop theoretical error bispectrum covariance, and the cross-covariance between the power spectrum and bispectrum (computed in perturbation theory), as well as if we replace the Gaussian bispectrum covariance with the sample covariance from the available mocks. All these different options yield statistically indistinguishable results.

Our total likelihood thus consists of a product of the bispectrum and baseline power spectrum likelihoods,

$$\mathcal{L}_{\rm tot} = \mathcal{L}_{\rm B}\times\mathcal{L}_{\rm P}. \tag{4.5}$$

The details of our baseline power spectrum likelihood can be found in Appendix D and in Ref. [77]. We compute power spectrum theoretical templates using the CLASS-PT code [44].[9] We run MCMC chains using the MONTEPYTHON code [103,104].[10] Posterior density plots are generated with the GETDIST package [105]. We will scan over the parameters of the base ΛCDM model and EFT nuisance parameters [53,54] (see Appendix D for precise definitions),

$$\{\omega_{\rm cdm}, H_0, A_s, n_s\} \times\{b_1, b_2, b_{\mathcal{G}_2}, b_{\Gamma_3}, C_0, C_2, C_4, b_4, a_0, a_2, P_{\rm shot}, B_{\rm shot}, c_1\}. \tag{4.6}$$

The priors on the power spectrum nuisance parameters are also given in Appendix D. As for $B_{\rm shot}$, we place a Gaussian

---

[9] Publicly available at https://github.com/Michalychforever/CLASS-PT.

[10] Publicly available at https://github.com/brinckmann/montepython_public.

prior on it with unit mean, which corresponds to the Poissonian sampling prediction, and unit variance,

$$B_{\rm shot} \sim \mathcal{N}(1, 1^2). \tag{4.7}$$

c_1 is varied in our MCMC chains without any priors, unless otherwise stated. We fix the physical baryon density to its true value in order to simulate the big bang nucleosynthesis (BBN) prior as it was used in Refs. [48,53].[11]

V. RESULTS

We start our analysis from the simple case of the real space bispectrum, which is free from redshift space distortions (RSD) and projection effects. Then, we will analyze a setup that closely matches an actual spectroscopic survey: we will study the bispectrum in redshift space and in the presence of the projection effect.

Since the PT challenge data which we are using is still ongoing, we report the measurements of all cosmological parameters normalized to their true injected values. As far as nonlinear bias parameters are concerned, we will present their values after the subtraction of the fiducial values extracted from our best-fit estimates from the most constraining baseline likelihood analysis. Specifically, we will report

$$\Delta b_2 \equiv b_2 - b_2^{\rm bf}, \qquad \Delta b_{\mathcal{G}_2} \equiv b_{\mathcal{G}_2} - b_{\mathcal{G}_2}^{\rm bf}, \tag{5.1}$$

where $b_2^{\rm bf}, b_{\mathcal{G}_2}^{\rm bf}$ are best-fit values extracted from the fiducial analysis of the redshift space power spectrum combined with the real space bispectrum at $k_{\rm max} = 0.08\ h/{\rm Mpc}$. This will be our best guess for the true values of these parameters.

We emphasize that except for Sec. V D, in all our analysis the scale cuts of the power spectrum likelihood are kept fixed. Only $k_{\rm max}$ of the bispectrum data is varied.

A. Redshift space power spectrum + real space bispectrum

We start with the real space bispectrum, which can be formally obtained from our model Eq. (3.14) by setting $f = 0$, $c_1 = 0$, and ignoring the AP effect. We also note that the discreteness weights are closer to unity in this case. This can be attributed to the absence of leakage from higher angular moments [79], which is present in the redshift-space case. We perform our analysis for the bispectrum for five choices of $k_{\rm max}$ ranging from 0.06 to 0.14 $h\,{\rm Mpc}^{-1}$ with a step 0.02 $h\,{\rm Mpc}^{-1}$. The resulting corner plot from our MCMC analyses is shown in Fig. 2, and the 1D marginalized limit for the case $k_{\rm max} = 0.08\ h\,{\rm Mpc}^{-1}$ are presented in Table I. The best fitting curves for certain triangle configurations are shown in Fig. 3, while Fig. 4 is a residual plot over all triangles used in the fit.

We observe that inclusion of the bispectrum sharpens estimates for all cosmological and bias parameters and does not lead to any significant biases up to $k_{\rm max} = 0.08\ h\,{\rm Mpc}^{-1}$. We see some small biases, especially in the $b_1 - \sigma_8$ plane, but our MCMC posteriors still enclose the true values within 99% C.L., which makes these shifts compatible with statistical fluctuations. Besides, these small shifts do not change when switching the bispectrum data cut from 0.06 to 0.08 $h\,{\rm Mpc}^{-1}$. In contrast, for $k_{\rm max} > 0.08\ h\,{\rm Mpc}^{-1}$ we see clear shifts that push estimated values away from the ground truth. In particular, we find the bias on σ_8 to be $[-1.9, -5.2, -6.7]\sigma$ for $k_{\rm max}/h{\rm Mpc}^{-1} = [0.1, 0.12, 0.14]$, respectively. This suggests us to adopt $k_{\rm max} = 0.08\ h\,{\rm Mpc}^{-1}$ as a baseline data cut for the real space bispectrum in what follows. Similar result is obtained in [12,13] for the joint fit of the real space power spectrum and the real space bispectrum.

The tree-level bispectrum likelihood improves constraints on cosmological and some nuisance parameters. This improvement can be estimated by ratios of the 1D marginalized 68% confidence intervals. For the cosmological parameters we have

$$\frac{\sigma_{\rm P+B}}{\sigma_{\rm P}}\{\omega_{\rm cdm}, h, n_s, A_s, \Omega_m, \sigma_8\} = \{0.82, 0.90, 0.81, 0.88, 0.83, 0.93\}$$

indicating a $(10-20)\%$ improvement in most cases. The gain is more sizable for the nuisance parameters,

$$\frac{\sigma_{\rm P+B}}{\sigma_{\rm P}}\{b_1, b_2, b_{\mathcal{G}_2}, P_{\rm shot}\} = \{0.75, 0.09, 0.07, 0.61\}.$$

Intuitively, this happens because in the bispectrum one can probe the galaxy bias parameters from large scales, and hence their determination is not contaminated by loop corrections and additional nuisance parameter marginalization.

The picture that we have observed here is in stark contrast with the real space only results, presented in Appendix E. This analysis shows that the real space power spectrum has much less information than the redshift-space one. In this case the combination with the bispectrum leads to a dramatic shrinking of posterior distributions for both cosmological and nuisance parameters. However, in redshift space the power spectrum has much more information to begin with, and thus the addition of the bispectrum yields only a moderate improvement.

---

[11] Formally, we also use the FIRAS value of the current CMB temperature T_0, which is a required input parameter in the Boltzmann code CLASS [106]. This parameter is tightly constrained by FIRAS and other probes, see e.g. [107] for more detail.

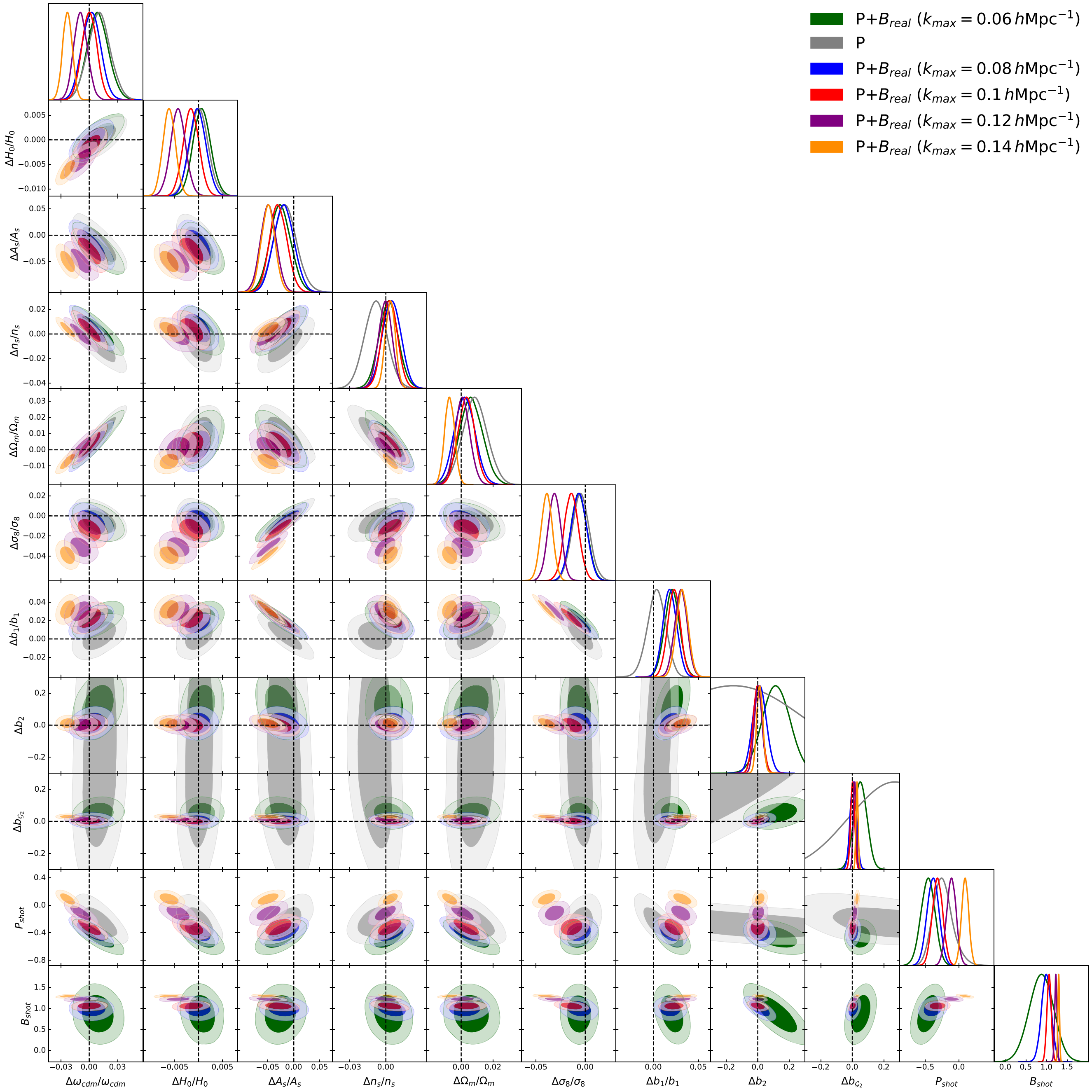

FIG. 2. Posterior distributions of cosmological and some nuisance parameters from MCMC analyses of the joint redshift-space power spectrum and real space bispectrum data. We show results for five different choices of the bispectrum data cut k_{max}. All cosmological parameters and b_1 are normalized to their true values. We have subtracted constant fiducial values from the quadratic bias parameters b_2 and $b_{\mathcal{G}_2}$. Results for the power spectrum data only are shown for comparison.

B. Bias parameters

Our simulated galaxies are produced with simple HOD models and therefore one may expect their nonlinear bias parameters to match those of the host halos and to follow the same dependence on b_1. Let us compare this expectations with reality (similar measurements in real space were done in [12,13]). For the tidal bias $b_{\mathcal{G}_2}$, as a first guess, we can use the so-called Lagrangian local in matter density (LLIMD) bias model prediction $b_{\mathcal{G}_2}^{\mathrm{LLIMD}} = -2(b_1 - 1)/7$ [71]. Using the fiducial value of b_1 we find

$$\Delta b_{\mathcal{G}_2}^{\mathrm{LLIMD}} = -\frac{2}{7}(b_1^{\mathrm{fid}} - 1) - b_{\mathcal{G}_2}^{\mathrm{fid}} = 0.23, \tag{5.2}$$

TABLE I. One-dimensional marginalized limit for the cosmological and most important nuisance parameters from various PT challenge likelihoods: redshift space power spectrum only (upper left panel), the joint power spectrum + real space bispectrum (upper right panel), redshift space bispectrum only (lower left panel), and the joint redshift space power spectrum + redshift space bispectrum (lower right panel). Parameters that were directly varied in MCMC chains are displayed in the upper part of the table, the lower groups contain derived parameters. Most parameters are normalized to their true values. See the main text for more detail.

Power	
Parameter	68% limits
$\Delta H_0/H_0$	0.0001 ± 0.0019
$\Delta\omega_{\rm cdm}/\omega_{\rm cdm}$	0.010 ± 0.012
$\Delta A_s/A_s$	-0.016 ± 0.022
$\Delta n_s/n_s$	-0.0084 ± 0.0094
$\Delta b_1/b_1$	0.003 ± 0.010
Δb_2	$-0.13^{+0.44}_{-0.51}$
$\Delta b_{\mathcal{G}_2}$	0.29 ± 0.30
$P_{\rm shot}$	$-0.24^{+0.12}_{-0.16}$
$\Delta\sigma_8/\sigma_8$	-0.0045 ± 0.0087
$\Delta\Omega_m/\Omega_m$	0.0087 ± 0.0077
$\frac{b_1^3\sigma_8^4}{(b_1^3\sigma_8^4)_{\rm fid}} - 1$	-0.008 ± 0.022

Power + real space bispectrum	
Parameter	68% limits
$\Delta H_0/H_0$	-0.0002 ± 0.0018
$\Delta\omega_{\rm cdm}/\omega_{\rm cdm}$	0.0022 ± 0.0098
$\Delta A_s/A_s$	-0.019 ± 0.019
$\Delta n_s/n_s$	0.0048 ± 0.0076
$\Delta b_1/b_1$	0.0183 ± 0.0077
Δb_2	0.011 ± 0.043
$\Delta b_{\mathcal{G}_2}$	0.006 ± 0.020
$P_{\rm shot}$	-0.384 ± 0.089
$B_{\rm shot}$	0.99 ± 0.12
$\Delta\sigma_8/\sigma_8$	-0.0065 ± 0.0080
$\Delta\Omega_m/\Omega_m$	0.0022 ± 0.0064
$\frac{b_1^3\sigma_8^4}{(b_1^3\sigma_8^4)_{\rm fid}} - 1$	0.028 ± 0.016

RSD bispectrum	
Parameter	68% limits
$\Delta H_0/H_0$	-0.026 ± 0.015
$\Delta\omega_{\rm cdm}/\omega_{\rm cdm}$	-0.026 ± 0.032
$\Delta A_s/A_s$	$-0.07^{+0.17}_{-0.35}$
$\Delta n_s/n_s$	-0.018 ± 0.034
$\Delta b_1/b_1$	$0.07^{+0.20}_{-0.26}$
Δb_2	$0.81^{+0.26}_{-0.33}$
$\Delta b_{\mathcal{G}_2}$	$0.270^{+0.068}_{-0.091}$
c_1	-2.4 ± 3.8
$P_{\rm shot}$	-0.095 ± 0.93
$B_{\rm shot}$	$0.89^{+0.69}_{-0.61}$
$\Delta\sigma_8/\sigma_8$	$-0.07^{+0.11}_{-0.16}$
$\Delta\Omega_m/\Omega_m$	$0.033^{+0.032}_{-0.039}$
$\frac{b_1^3\sigma_8^4}{(b_1^3\sigma_8^4)_{\rm fid}} - 1$	$-0.194^{+0.082}_{-0.074}$

(Table continued)

TABLE I. *(Continued)*

Power + RSD bispectrum	
Parameter	68% limits
$\Delta H_0/H_0$	-0.0014 ± 0.0018
$\Delta\omega_{\rm cdm}/\omega_{\rm cdm}$	-0.005 ± 0.010
$\Delta A_s/A_s$	-0.017 ± 0.021
$\Delta n_s/n_s$	0.0036 ± 0.0080
$\Delta b_1/b_1$	0.0149 ± 0.0085
Δb_2	-0.054 ± 0.088
$\Delta b_{\mathcal{G}_2}$	0.070 ± 0.026
c_1	5.6 ± 2.7
$P_{\rm shot}$	-0.249 ± 0.093
$B_{\rm shot}$	1.75 ± 0.43
$\Delta\sigma_8/\sigma_8$	-0.0107 ± 0.0082
$\Delta\Omega_m/\Omega_m$	-0.0017 ± 0.0068
$\frac{b_1^3\sigma_8^4}{(b_1^3\sigma_8^4)_{\rm fid}} - 1$	0.001 ± 0.016

which is more that 10σ away from the truth. The LLIMD approximation is known to be in tension with high precision simulation measurements, which clearly show the evidence for the tidal Lagrangian bias [108]. A better fit to this data is a coevolution model with the initial Lagrangian bias that has the following dependence on the mean halo mass M

$$b^L_{\mathcal{G}_2} = -0.5\left(\frac{M}{4\times 10^{14}\,h^{-1}\,M_\odot}\right)^{0.8}. \qquad (5.3)$$

Reference [108] also presents the function $M(b_1)$, from which we can express the above equation as $b^L_{\mathcal{G}_2}(b_1)$. Inserting there our measurement of b_1, we find

$$\Delta b^{\rm LTCM}_{\mathcal{G}_2} = -\frac{2}{7}(b_1^{\rm fid} - 1) + b^L_{\mathcal{G}_2}(b_1^{\rm fid}) - b^{\rm fid}_{\mathcal{G}_2} = 0.072, \qquad (5.4)$$

where “LTCM” stands for “Lagrangian tidal coevolution model.” We see that our measurement is still in $\sim 3\sigma$ tension with the prediction of LTCM, although in absolute terms the discrepancy is quite small. The discrepancy with the excursion set prediction from Ref. [109] is also quite high, it exceeds 10σ in terms of the standard deviation of our measurement.

As far as b_2 is concerned, we can compare our measurement with the fit to halos from Refs. [110,111], i.e. to consider

$$\Delta b_2^{\mathrm{halo}} = b_2^{\mathrm{halo}}(b_1^{\mathrm{fid}}, b_{\mathcal{G}_2}^{\mathrm{fid}}) - b_2^{\mathrm{fid}} = -0.49, \qquad (5.5)$$

where

$$b_2^{\mathrm{halo}}(b_1, b_{\mathcal{G}_2}) = 0.412 - 2.143 b_1 + 0.929 b_1^2 + 0.008 b_1^3 + \frac{4}{3} b_{\mathcal{G}_2}. \qquad (5.6)$$

Note that we have accounted for the difference in our definition of quadratic biases with respect to Refs. [110,111],

$$b_{\mathcal{G}_2}^{\text{this work}} = b_{\mathcal{G}_2}^{\text{previous}}, \qquad b_2^{\text{this work}} = b_2^{\text{previous}} + \frac{4}{3} b_{\mathcal{G}_2}^{\text{this work}}. \qquad (5.7)$$

Thus, our analysis confirms significant deviations between the bias coefficients of galaxies and halos, which have already been pointed out in the literature [12,13,112]. We also confirm the trend seen in the literature for the CMASS-like galaxies [47] (similar to our PT challenge sample): the tidal bias of galaxies is lower than that of halos, but b_2 is higher. In particular, the results of Ref. [12] for the CMASS galaxies read

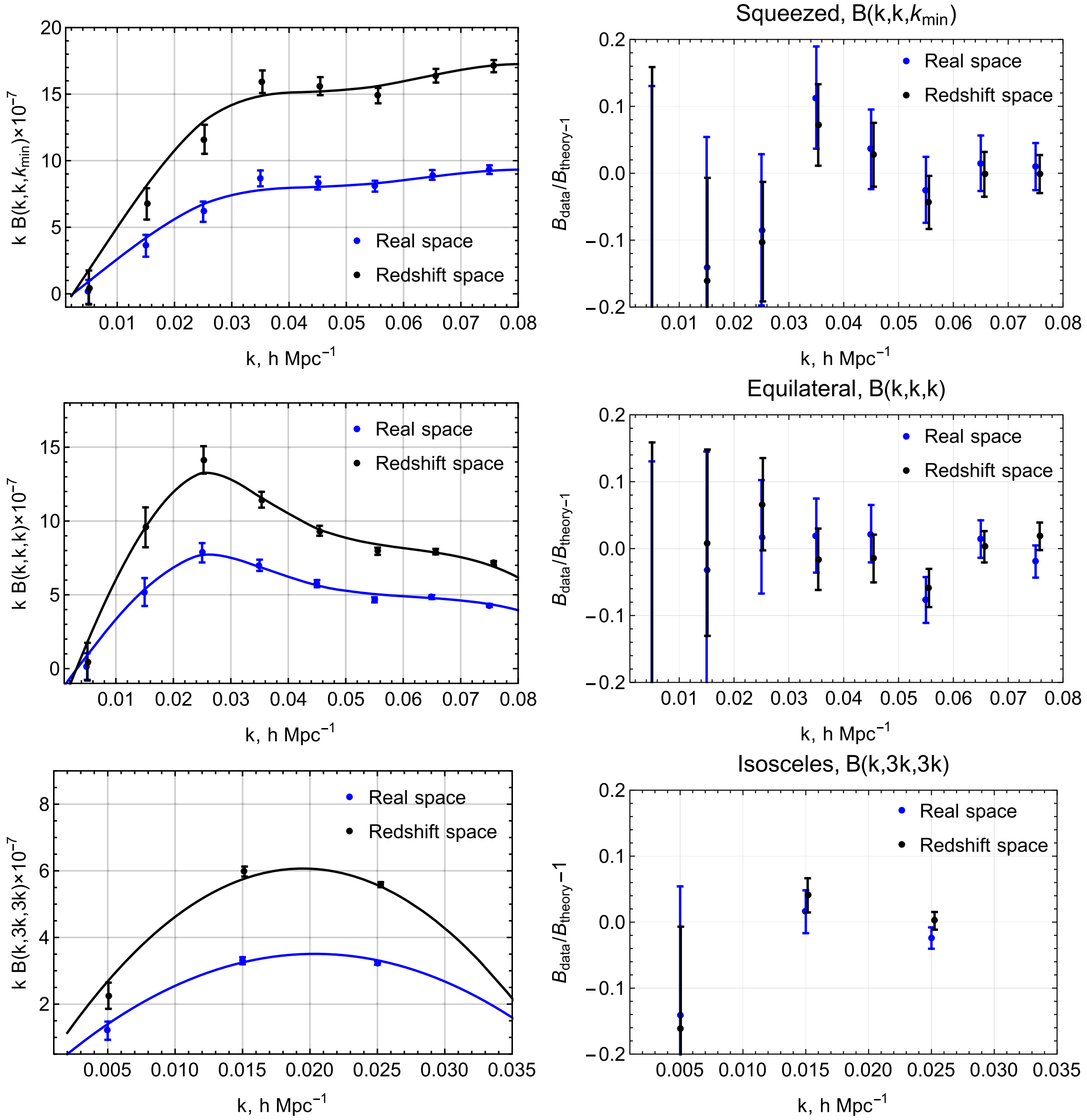

FIG. 3. Bispectrum data points from the PT challenge simulations along with best-fit theoretical predictions extracted from our MCMC chains. We show the bispectra for squeezed, equilateral, and isosceles triangles (left panels), and the corresponding residuals (right panels).

$$b_2^{\rm gal} = -0.2 \pm 0.1, \qquad b_{\mathcal{G}_2}^{\rm gal} = -0.46 \pm 0.06. \tag{5.8}$$

These values can be compared with the predictions of the local Lagrangian approximation and the fit to b_2,

$$\begin{aligned}\text{Ref. [12]}: \Delta b_2 &= b_2^{\rm halo}(b_2^{\rm gal}, b_{\mathcal{G}_2}^{\rm gal}) - b_2^{\rm gal} = -0.41 \pm 0.1,\\ \Delta b_{\mathcal{G}_2} &= b_{\mathcal{G}_2}^{\rm LLIMD} - b_{\mathcal{G}_2}^{\rm gal} = 0.17 \pm 0.06.\end{aligned} \tag{5.9}$$

These estimates perfectly agree with our results

$$\Delta b_2 = -0.49 \pm 0.04, \qquad \Delta b_{\mathcal{G}_2} = 0.23 \pm 0.02. \tag{5.10}$$

Finally, let us discuss the cubic tidal bias parameter b_{Γ_3}. At the power spectrum level it is almost fully degenerate with $b_{\mathcal{G}_2}$. However, this degeneracy gets broken by the bispectrum data, since only $b_{\mathcal{G}_2}$ enters the tree-level bispectrum model. We will compare our measurements with halo relations obtained in Refs. [108,109],

$$\begin{aligned}\text{Ref. [108]}: b_{\Gamma_3}^{\rm halo} &= -b_{\mathcal{G}_2} - \frac{1}{15}(b_1 - 1),\\ \text{Ref. [109]}: b_{\Gamma_3}^{\rm halo} &= -\frac{1}{6}(b_1 - 1) - \frac{3}{2} b_{\mathcal{G}_2}.\end{aligned} \tag{5.11}$$

This gives us a tension between our results and these halo predictions at the 2σ level,

$$\begin{aligned}\text{Ref. [108]}: b_{\Gamma_3}^{\rm gal} - b_{\Gamma_3}^{\rm halo}(b_1^{\rm gal}, b_{\mathcal{G}_2}^{\rm gal}) &= 0.23 \pm 0.11,\\ \text{Ref. [109]}: b_{\Gamma_3}^{\rm gal} - b_{\Gamma_3}^{\rm halo}(b_1^{\rm gal}, b_{\mathcal{G}_2}^{\rm gal}) &= 0.24 \pm 0.11.\end{aligned} \tag{5.12}$$

However, here we see the difference with respect to the CMASS-like sample of Ref. [12] ($b_{\Gamma_3} = -7\gamma_{21}/4$ in their notation). The relevant measurement from this work is fully consistent with that of halos,

$$b_{\Gamma_3}^{\rm CMASS} - b_{\Gamma_3}^{\rm halo}(b_1^{\rm gal}, b_{\mathcal{G}_2}^{\rm gal}) = -0.02 \pm 0.14. \tag{5.13}$$

The discrepancy between our b_{Γ_3} and that of Ref. [12] is marginally below 2σ, and hence our measurements can be considered consistent.

Overall, we conclude that with the PT challenge simulations we see a $\sim 3\sigma$ discrepancy between the bias parameters of our HOD galaxies and their host halos. However, our bias parameter measurements agree well with those from similar mock CMASS-like galaxies, analyzed in Ref. [12].

C. Redshift space

We now consider the realistic case of the redshift-space bispectrum monopole in the presence of the AP effect. We analyze our joint power spectrum and bispectrum likelihoods for three choices of the bispectrum data cut ranging $k_{\rm max}$ from 0.08 to 0.12 $h\,{\rm Mpc}^{-1}$ with a step 0.02 $h\,{\rm Mpc}^{-1}$. Our triangle plot is displayed in Fig. 5, where for comparison we also show the results of the baseline real space bispectrum analysis from the previous section. Marginalized 1D limits are presented in Table I. Best-fit curves and the residual plot are shown in Figs. 3 and 4.

We see that at $k_{\rm max} = 0.08\ h\,{\rm Mpc}^{-1}$ the addition of the bispectrum likelihood slightly narrows the power spectrum contours and does not lead to any significant bias. Both cosmological and nuisance parameters are recovered within 95% confidence intervals. However, already at $k_{\rm max} = 0.08\ h\,{\rm Mpc}^{-1}$ we observe some evidence for the nonzero FOG counterterm c_1, which suggests that the one-loop corrections may not be negligible. Indeed, for more aggressive data cuts $k_{\rm max} > 0.08\ h\,{\rm Mpc}^{-1}$ we find large biases that signal the breakdown of the tree-level bispectrum model. These biases are more significant than those that we have seen in the real space power spectrum likelihood, which is an expected consequence of nonlinear redshift space distortions [41,46,54,65,113,114]. A similar conclusion that FOGs in the bispectrum are important even on relatively large scales was made in Ref. [115].

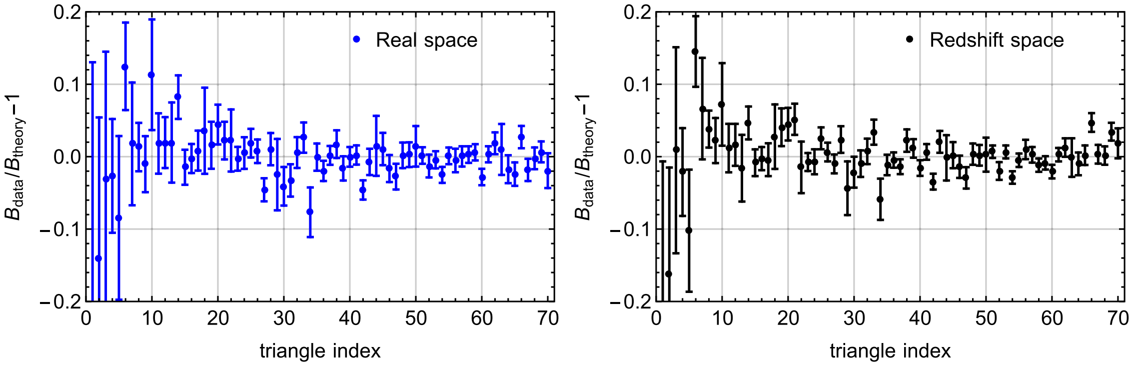

FIG. 4. Residuals between the bispectrum data and best-fitting theory templates for all triangles from the real space (left panel) and the redshift space (right panel) analyses.

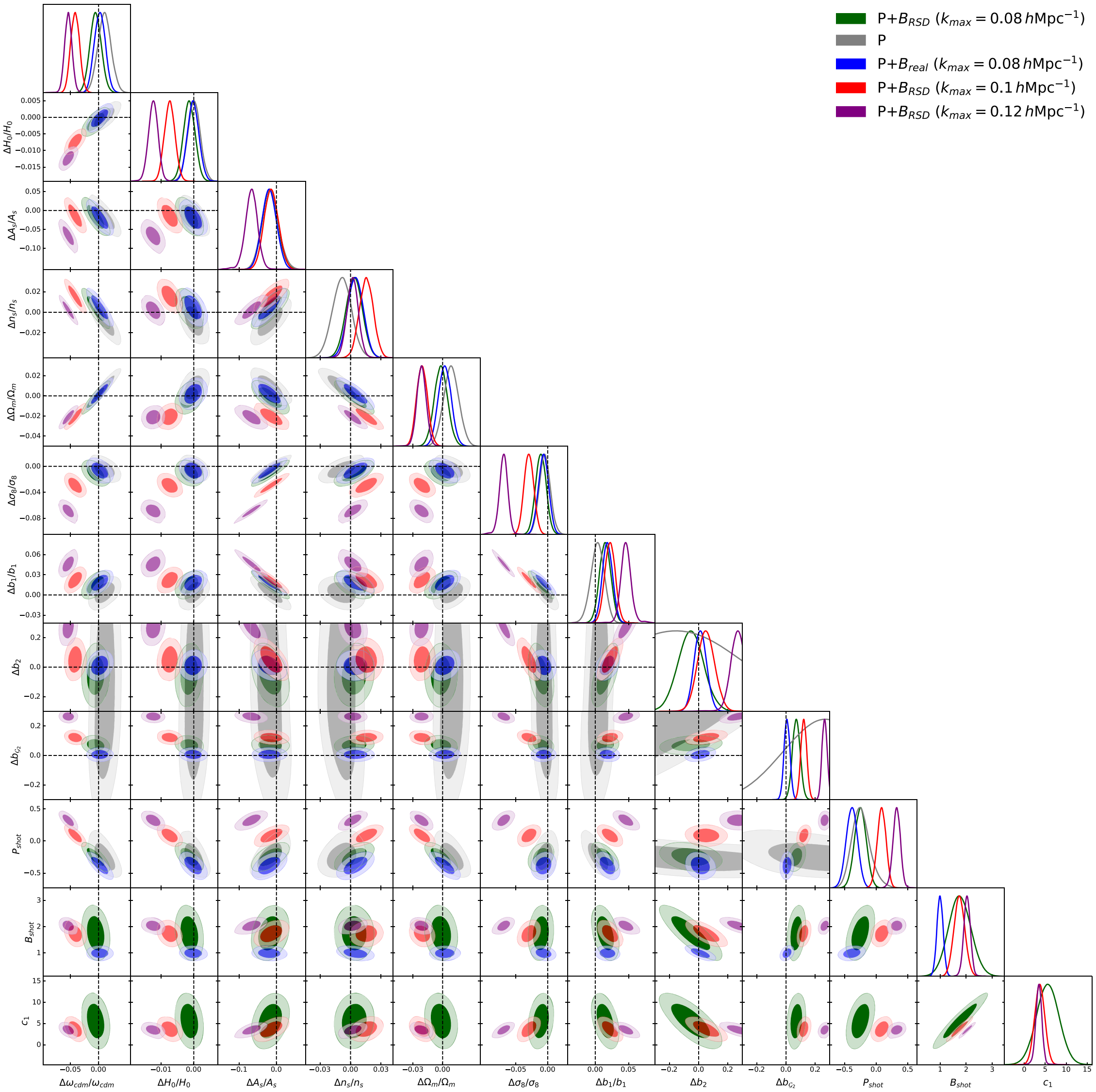

FIG. 5. Posterior distributions of cosmological and certain nuisance parameters from MCMC analyses of the joint redshift space power spectrum and redshift space bispectrum monopole data. We show results for three different choices of the bispectrum data cut k_{max}. All cosmological parameters and b_1 are normalized to their true values. We have subtracted constant fiducial values from the quadratic bias parameters b_2 and $b_{\mathcal{G}_2}$. Results for the power spectrum ("P") and for the power spectrum + real space bispectrum ["$P + B_{\mathrm{real}}(k_{\mathrm{max}} = 0.08\ h\,\mathrm{Mpc}^{-1})$"] datasets are shown for comparison.

These results motivate us to choose $k_{\mathrm{max}} = 0.08\ h\,\mathrm{Mpc}^{-1}$ as our baseline data cut.

In Fig. 6 and Table I we display the breakdown of different likelihoods in terms of their parameter constraints, including the redshift space bispectrum alone. Clearly, the constraints on cosmological parameters are heavily dominated by the power spectrum data. In part, this is a result of using only relatively low wave numbers in our bispectrum analysis.

The bispectrum likelihood adds new information mostly through the bias parameter measurements. In particular, the principle component of the $b_1 - \sigma_8$ degeneracy can be well approximated by a combination $b_1^3\sigma_8^4$, which captures the galaxy bispectrum amplitude in the absence of quadratic biases and projection effects. Our redshift space bispectrum-only analysis yields a measurement quite competitive with the redshift-space power spectrum result,[12] cf. Table I. Beside $b_1 - \sigma_8$, the bispectrum also adds significant information through the quadratic bias parameters b_2 and $b_{\mathcal{G}_2}$, whose measurements from the bispectrum alone are more precise than from the power spectrum.

---

[12] For the power spectrum the principle component is slightly different, $b_1^2\sigma_8^4$. This small difference in the exponent is not important for our discussion.

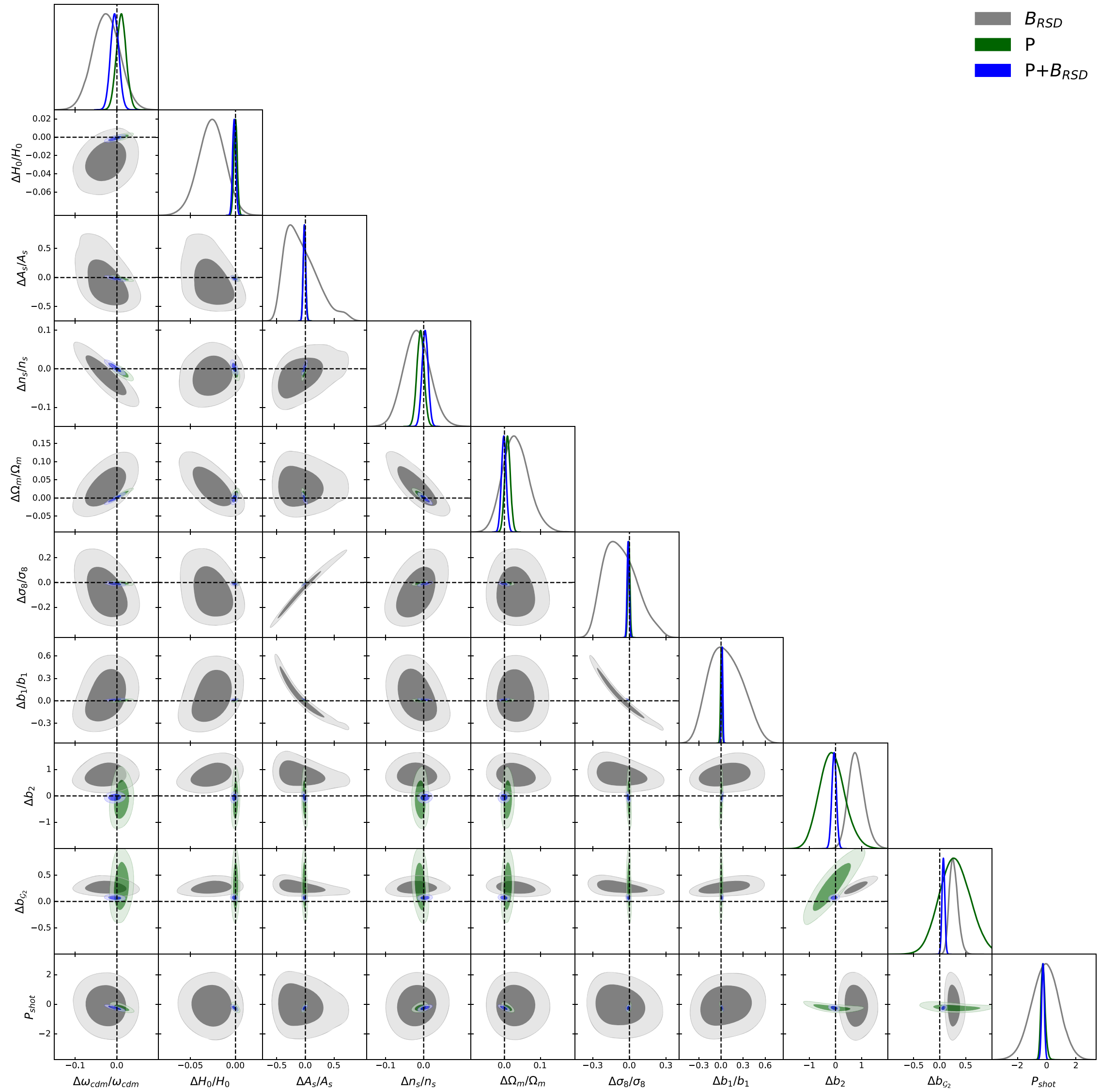

FIG. 6. Posterior distributions of cosmological and certain nuisance parameters from MCMC analyses of the redshift space power spectrum, redshift space bispectrum, and their combination. We use $k_{\max} = 0.08\ h\,\mathrm{Mpc}^{-1}$ for the bispectrum here.

Addition of the bispectrum leads to following improvements on cosmological and nuisance parameters

$$\frac{\sigma_{\mathrm{P+B}}}{\sigma_{\mathrm{P}}}\{\omega_{\mathrm{cdm}}, h, n_s, A_s, \Omega_m, \sigma_8\} = \{0.88, 0.94, 0.86, 0.95, 0.89, 0.96\},$$
$$\frac{\sigma_{\mathrm{P+B}}}{\sigma_{\mathrm{P}}}\{b_1, b_2, b_{\mathcal{G}_2}, P_{\mathrm{shot}}\} = \{0.84, 0.18, 0.09, 0.65\}. \tag{5.14}$$

In general, the gain here is more modest compared to what we have obtained from the real space bispectrum. One reason for that is the correlation between the additional FOG counterterm c_1 and other parameters. For example, the degeneracy between c_1 and b_2, B_{shot} is quite significant, which explains why the confidence intervals for these nuisance parameters are noticeably larger than those of the real space bispectrum case. Another reason for the relatively small improvement in cosmological parameters is that the BAO wiggles are more suppressed in redshift space, cf. Eq. (3.12), and hence there is less available distance information.

All in all, the upshot of our analysis is that for the full PT challenge simulation volume the data cut for the tree-level redshift-space bispectrum model is $k_{\max} = 0.08\ h\,\mathrm{Mpc}^{-1}$, and the addition of the bispectrum likelihood yields $\lesssim 10\%$ improvement on cosmological parameters, but much larger gains on bias parameters.

D. Forecast for BOSS

It is useful to rerun our analysis for the covariance that matches the volume of the currently available BOSS data.

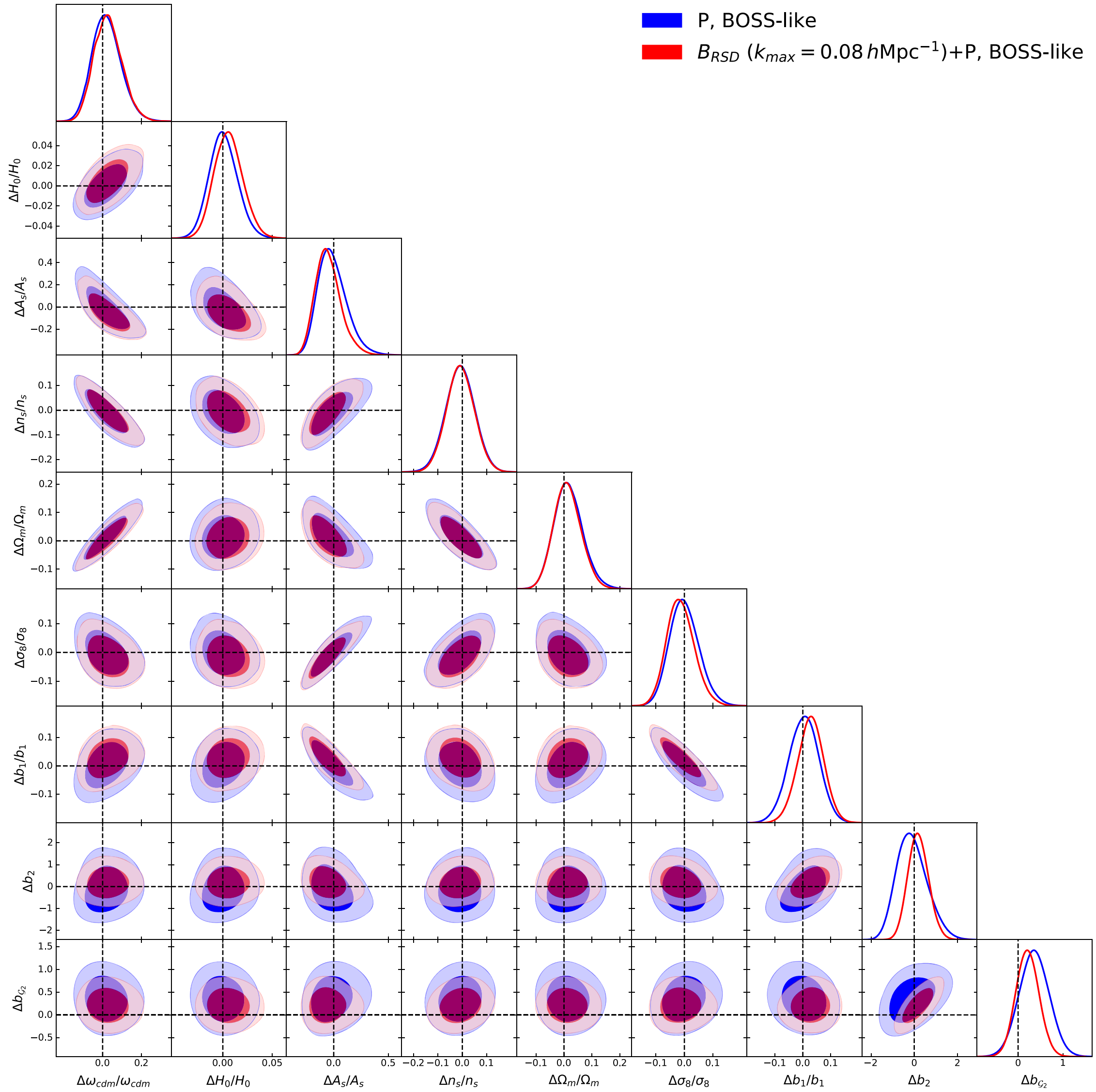

FIG. 7. Same as Fig. 5 but with the covariance rescaled by 100 to match the BOSS survey volume.

In this case the covariance is larger, and hence we can use more aggressive data cuts provided that the bias in cosmological parameters due to higher order loop corrections is smaller than a fraction of the statistical error. In this case the power spectrum multipole analysis can be pushed to $k_{\max} = 0.20\ h\,\mathrm{Mpc}^{-1}$, which is noticeably larger than our baseline PT challenge power spectrum multipole data cut $k_{\max} = 0.14\ h\,\mathrm{Mpc}^{-1}$ [53]. Note that this $k_{\max}$ is lower than $k_{\max} = 0.25\ h\,\mathrm{Mpc}^{-1}$ used in Refs. [48,116] because here we include the hexadecapole moment, see Ref. [53] for more detail. Consequently, the transverse power spectrum moment Q_0 is taken in the range $0.2 < k/(h\mathrm{Mpc}^{-1}) < 0.4$ [77]. Unfortunately, we cannot push the bispectrum analysis to $k_{\max} = 0.1\ h\,\mathrm{Mpc}^{-1}$ because the relative theory systematic error on σ_8 there is around 3%. This is a significant fraction of the BOSS statistical error, $\sigma_{\sigma_8}/\sigma_8 \approx 5\%$. We have explicitly checked that the recovered value of σ_8 is biased by 1σ of the BOSS error when the bispectrum is taken at $k_{\max} = 0.1\ h\,\mathrm{Mpc}^{-1}$. Therefore, we proceed with the same baseline cut as in the PT challenge analysis of the previous section, $k_{\max} = 0.08\ h\,\mathrm{Mpc}^{-1}$.

We analyze the same PT challenge data but with the covariance rescaled by a factor 100, which is the difference between the PT challenge volume and the BOSS survey volume $V_{\mathrm{BOSS}} \simeq 6\ h^{-3}\,\mathrm{Gpc}^3$. In this particular analysis, we also impose the following Gaussian prior on c_1,

$$c_1 \sim \mathcal{N}(0, 5^2), \tag{5.15}$$

which is motivated by the EFT expectation $c_1 = \mathcal{O}(1)$. Our results are shown in Fig. 7 and in Table II.

TABLE II. 1D marginalized limits from analyses of the redshift space galaxy power spectrum (left panel) and the joint power and bispectrum data (right panel) from the PT challenge simulation with the covariance rescaled to match the volume of the BOSS survey, as shown in Fig. 7.

Power spectrum (PS), BOSS-like	
Parameter	68% limits
$\Delta H_0/H_0$	$0.001^{+0.013}_{-0.015}$
$\Delta\omega_{\rm cdm}/\omega_{\rm cdm}$	$0.021^{+0.065}_{-0.080}$
$\Delta A_s/A_s$	$-0.01^{+0.10}_{-0.15}$
$\Delta n_s/n_s$	-0.009 ± 0.059
$\Delta b_1/b_1$	0.004 ± 0.053
Δb_2	$-0.09^{+0.59}_{-0.80}$
$\Delta b_{\mathcal{G}_2}$	0.36 ± 0.33
$P_{\rm shot}$	-0.13 ± 0.51
$\Delta\sigma_8/\sigma_8$	$0.000^{+0.046}_{-0.055}$
$\Delta\Omega_m/\Omega_m$	$0.016^{+0.046}_{-0.055}$

PS + bispectrum, BOSS-like	
Parameter	68% limits
$\Delta H_0/H_0$	$0.006^{+0.013}_{-0.015}$
$\Delta\omega_{\rm cdm}/\omega_{\rm cdm}$	$0.029^{+0.063}_{-0.080}$
$\Delta A_s/A_s$	$-0.049^{+0.093}_{-0.13}$
$\Delta n_s/n_s$	-0.008 ± 0.057
$\Delta b_1/b_1$	0.028 ± 0.047
Δb_2	$0.19^{+0.44}_{-0.50}$
$\Delta b_{\mathcal{G}_2}$	0.21 ± 0.25
$P_{\rm shot}$	-0.38 ± 0.40
$B_{\rm shot}$	1.23 ± 0.89
c_1	0.1 ± 4.8
$\Delta\sigma_8/\sigma_8$	$-0.013^{+0.044}_{-0.052}$
$\Delta\Omega_m/\Omega_m$	$0.012^{+0.045}_{-0.052}$

We observe that the addition of the bispectrum has roughly the same impact for cosmological parameters are the full PT challenge case, i.e. there is a ∼10% improvement on the 1D marginalized constraint on A_s and σ_8, and barely any effect on other parameters. As far as quadratic bias parameters are concerned, the improvements for them are less sizable. In contrast to the full PT challenge simulation, in the BOSS-like power spectrum case the bias parameters are dominated by priors (given in Appendix D) and not by the data. Hence, the power spectrum posteriors are narrower to begin with. Still, the addition of the bispectrum data sharpens b_2 and $b_{\mathcal{G}_2}$ posteriors by a factor of two.

VI. COMPARISON WITH PREVIOUS WORK

Our analysis complements and extends other works on the galaxy bispectrum. Therefore, it is useful to compare our study with the most relevant literature.

Reference [11] studied the real space halo galaxy bispectrum from simulations with the overall volume similar to that of the PT challenge suite. This work used the tree-level bispectrum model to fit the pure bispectrum data (in the absence of the power spectrum), and has established that this model works up to $k_{\rm max} = 0.082\ h\,{\rm Mpc}^{-1}$, in agreement with our baseline result $k_{\rm max} = 0.08\ h\,{\rm Mpc}^{-1}$. This work did not find any significant deviations from Poissonian sampling for the halo bispectrum. Reference [13] used the same data to perform a joint power spectrum and bispectrum analysis in real space. When comparison is possible, our results agree. In particular, we find similar improvements on cosmological parameters for the real space analysis and find the sub-Poissonian shot noise for the PT challenge galaxies, both in real and redshift space. This detection is mainly driven by the power spectrum data, which yields a $\gtrsim 2\sigma$ deviation from the Poissonian sampling even in the absence of any bispectrum data. This can be compared with the bispectrum data alone (see Fig. 6), which is not precise enough to constrain the shot noise. When the two likelihoods are combined, we obtain much tighter constraints on the shot noise parameters than the bispectrum alone. This result is not surprising, given that on general grounds we do expect halo stochasticity to be different from that of galaxies, see e.g. [114]. The importance of beyond-Poissonian sampling for primordial non-Gaussianity constraints from the bispectrum was also emphasized in [10].

Reference [12] presented constraints on the galaxy bias parameters from the combination of the real space power spectrum and bispectrum data. This work used a one-loop theoretical error model for the bispectrum, which allowed one to push the analysis to small scales and achieve parameter measurement precision similar to ours while using smaller effective volume $V_{\rm eff} = 6\ h^{-3}\,{\rm Gpc}^3$. An important observation is our analysis confirms the result of Ref. [12] that the quadratic bias parameters of BOSS-like galaxies do not follow halo-calibrated dependencies on linear bias b_1. The deviations from these dependencies that we find in our work agree very well with those reported in Ref. [12].

It is very important to compare conclusions on the cosmological parameter improvements from the bispectrum in real space from Refs. [12,13] and from our redshift space analysis. References [12,13] showed that constraints on A_s typically improve by factors of 4–6 in real space. This improvement factor stays roughly the same regardless of whether the tree-level or the one-loop bispectrum model is used. In contrast to this, our analysis implies that the bispectrum monopole sharpens the A_s constraints only by ∼20% in redshift space. This happens because the notorious degeneracy between the linear bias b_1 and A_s, which plagues real space analyses, is lifted in redshift space already at the level of power spectrum multipoles.

The bispectrum monopole of BOSS-like mocks and the actual bispectrum data from the CMASS north galactic cap sample were analyzed in Ref. [49]. This analysis is closest to ours since it uses essentially a similar EFT theoretical model for the power spectrum part. However, its bispectrum analysis is different from ours by a number of instances. First, systematic errors in the window function treatment forced Ref. [49] to discard low wave number modes, i.e. use $k_{\mathrm{min}} = 0.04\ h\,\mathrm{Mpc}^{-1}$.[13] Second, similarly to us, the authors of Ref. [49] used the tree-level EFT model for the bispectrum monopole. However, they ignored IR resummation (which is necessary already at the tree level [4,63,73]) and additional corrections due to FOG and binning, which was partly justified by the smallness of the total simulation volume of that work compared to ours. Nevertheless, the final scale cuts $k_{\mathrm{max}} = (0.08\text{–}0.1)\ h\,\mathrm{Mpc}^{-1}$ of the bispectrum analysis of Ref. [49] are consistent with our choice $k_{\mathrm{max}} = 0.08\ h\,\mathrm{Mpc}^{-1}$. Finally, Ref. [49] found that the bispectrum data from one BOSS data chunk (CMASS north galactic cap) sharpens the constrain on A_s by $\lesssim 20\%$ and leaves intact other cosmological parameters. We have found a quantitatively similar behavior in our analysis, see Fig. 7. It will be interesting to see how much the constraints improve in the analysis of the actual BOSS data with our likelihood. We leave this for future work [119].

Finally, it is worth comparing our results with those from the MCMC forecast for the Euclid-like survey from Ref. [6]. This work used a very similar methodology and found that the addition of the tree-level bispectrum monopole likelihood leads to $\sim(10\text{–}50)\%$ on all relevant cosmological parameters of the ΛCDM model with massive neutrinos. Our analysis is different from Ref. [6] in several aspects. First, unlike Ref. [6], our baseline power spectrum likelihood contains the real space power spectrum Q_0 [77]. Moreover, our likelihood here includes physical priors on nuisance parameters, whereas Ref. [6] did not assume any priors on them. These two factors may diminish relative information content of the bispectrum in our work. Second, we analyze only one redshift bin here, whereas Ref. [6] considers a more realistic data sample spread across eight different bins. Clearly, this latter case contains more distance information that can be extracted through the AP effect. Third, we impose the BBN prior on Ω_b here, while Ref. [6] fits this parameter directly from the large-scale structure data. Despite these significant differences, one observes a qualitative agreement between our results: in both cases the tree-level bispectrum monopole improves cosmological parameter constrains by tens of percent.

VII. CONCLUSIONS

In this work we have studied the cosmological information present in the redshift-space bispectrum monopole of PT challenge simulation galaxies. We analyze the joint power spectrum and bispectrum likelihood using the one-loop EFT model for the power spectrum and the tree-level model for the bispectrum. This is a fully consistent approach as for both statistics we use the perturbative density field expanded to third order in the linear solution. Our bispectrum theoretical templates include, for the first time, all the effects that are needed to describe the data at this order: tree-level IR resummation, corrections due to discreteness, FOG, and the AP effect. Our main results are

(i) The tree-level bispectrum model is valid up to $k_{\mathrm{max}} = 0.08\ h\,\mathrm{Mpc}^{-1}$ for a BOSS-like luminous red galaxy sample.
(ii) The addition of the tree-level bispectrum likelihood to the power spectrum one leads to moderate improvements of constraints on cosmological parameters by $\lesssim 10\%$.
(iii) The improvement on bias parameters is very significant. The error bars on the quadratic local in density bias b_2 and the tidal bias $b_{\mathcal{G}_2}$ shrink by more than a factor of 10 after adding the bispectrum data.
(iv) We have found that the quadratic galaxy bias parameters are quite different from biases of host dark matter halos. This confirms the trend seen in the literature [12,112].

On the technical side, we have proposed a new efficient approach to account for binning effects by a combination of the integral approximation and discreteness weights, and also studied in detail the dependence of our results on bispectrum covariance matrix choices.

There are several ways to extend our analysis. First, it would be important to upgrade our theory model with the redshift-space one-loop bispectrum calculations. In particular, we have found that at $k_{\mathrm{max}} > 0.08\ h\,\mathrm{Mpc}^{-1}$ the data shows evidence for FOG, which is a loop effect in the EFT nomenclature. Given that the one-loop calculation significantly extends the regime of validity of the EFT in the power spectrum case, one may expect that a similar improvement can take place for the bispectrum. It is important to notice that for consistency one needs to compute the power spectrum at two-loop order when considering the one-loop bispectrum.

Moreover, it is also interesting to consider higher angular moments of the redshift-space bispectrum. Various forecasts suggest that these moments may contain significant cosmological information, see e.g. [5]. We plan to verify these results in an actual analysis of simulated or real data. Importantly, higher order bispectrum multipoles are sensitive to FOG, and hence one-loop corrections are desirable for their systematic study. This issue can be mitigated with an analog of the transverse moment Q_0 for the bispectrum. We plan to study this statistics in future.

Another natural step is the analysis of the actual bispectum data from the BOSS survey [119]. Our work suggests that the inclusion of the bispectrum may improve

---

[13] In principle, this issue can be avoided with the help of unwinnowed estimators implemented along the lines of Refs. [117,118].

constraints on the mass fluctuation amplitude by ∼10%. This improvement is not very dramatic, but it should be pointed out that so far we have considered only the minimal ΛCDM model. The information content of the redshift space bispectrum can be richer in nonminimal cosmological models, which may have some implications for certain tensions, e.g. the so-called σ_8 tension [120].

Finally, it would be interesting to repeat our analysis for the emission line galaxies, which will be the main targets of future surveys like DESI [121] and Euclid [122,123]. Emission line galaxies are less biased than the red luminous galaxies whose mocks we studied in this paper. Moreover, recent measurements suggest that they are less affected by FOG [90,124], which implies that the EFT model may perform better for this sample.

ACKNOWLEDGMENTS

We thank Giovanni Cabass, Roman Scoccimarro, and Jay Wadekar for fruitful discussions. The work of M. M. I. has been supported by NASA through the NASA Hubble Fellowship Grant No. HST-HF2-51483.001-A awarded by the Space Telescope Science Institute, which is operated by the Association of Universities for Research in Astronomy, Incorporated, under NASA Contract No. NAS5-26555. O. H. E. P. thanks the Simons Foundation for support. This work was supported in part by MEXT/JSPS KAKENHI Grants No. JP19H00677, No. JP20H05861, and No. JP21H01081. We also acknowledge financial support from Japan Science and Technology Agency (JST) AIP Acceleration Research Grant No. JP20317829. The simulation data analysis was performed partly on Cray XC50 at Center for Computational Astrophysics, National Astronomical Observatory of Japan.

APPENDIX A: TESTS OF BINNING

In order to account for binning effects, one should ideally evaluate the full sum over all possible triangle configurations inside the bin. However, this evaluation is computationally very expensive. In the main text we have used the integral approximation along with discreteness weights that correct for the inaccuracy of this approximation for the folded triangles. In this appendix we present an alternative to this scheme, which works well for the real space bispectrum.

The main goal of our binning scheme is to generate many “fundamental” triangle configurations based on the true k_f and then sum them into appropriate bins. It is computationally expensive to generate all the fundamental triangles on the actual 3D Fourier grid. Moreover, it is also not efficient, because the fundamental grid contains a large number of identical fundamental triangles. We can avoid that by organizing a sum over *unique* fundamental triangle configurations with $q_1 \geq q_2 \geq q_3$, where q_i are wave vector moduli of fundamental triangles. In this case we need to sample the bispectra over a relatively small grid of wave numbers. We will call this method “approximate 1D binning” in what follows. It is based, essentially, on taking the integral expression Eq. (3.26) and approximating it with a sum over appropriate discrete configurations of wave vector moduli.

Let us start with the integral approximation Eq. (3.26), obtained after eliminating most of angular variables by means of the Dirac delta function. In real space the integrals over μ and ϕ drop out of this expression because the bispectrum does not depend on angles. Now we can write down the following discrete approximation to the final integral,

$$\hat{B}_0^{\rm int} \simeq \frac{V\sum_{123} q_1 q_2 q_3 B(q_1,q_2,q_3)}{V\sum_{123} q_1 q_2 q_3 1}, \tag{A1}$$

where the sum $\sum_{123}$ is taken over all configurations of momentum moduli q_i that fall in the bin. This sum contains many indistinguishable modes. Now we replace this sum with a discrete sum over independent triangle configurations only,

$$\hat{B}_0^{\rm int} \simeq \frac{V\sum_T q_1 q_2 q_3 B(q_1,q_2,q_3)}{V\sum_T q_1 q_2 q_3 1}, \tag{A2}$$

where the sum $\sum_T$ runs over all unique triangles that fall in the bin (k_1, k_2, k_3) and that respect the k_f spacing,

$$\sum_T \equiv \sum_{q_1=\max(k_f,k_1-\Delta k/2)}^{k_1+\Delta k/2} \; \sum_{q_2=\max(k_f,k_2-\Delta k/2)}^{\min(k_2+\Delta k/2,q_1)} \; \sum_{q_3=\max(k_f,k_3-\Delta k/2,q_1-q_2)}^{\min(k_3+\Delta k/2,q_2)}. \tag{A3}$$

To compute the sum in Eq. (A2) in practice, we generate a grid of tuples (q_1, q_2, q_3) with spacing $\Delta q = k_f$ and select only those that satisfy the constraints of Eq. (A3) for each bin (k_1, k_2, k_3). Notice that we have used the isotropy of the bispectrum in our derivation, which is certainty not true in redshift space. We apply the approximate 1D binning scheme in real space only.

Equation (A2) is not exact because it was derived from the integral expression (3.26), which is approximate on its own. But we can still use it as an alternative prescription for the binning effects that will allow us to assess the systematic error of our baseline discreteness weight method. The two methods can be compared in Fig. 8, “Baseline” vs “Approx 1D binning.” We can clearly see that they yield almost identical results. This validates our discreteness weight approach adopted in the main analysis. In this plot, we also show results from the “pure integral approximation” obtained from the bispectrum model with the integral approximation but without discreteness weights or any additional corrections. This prescription

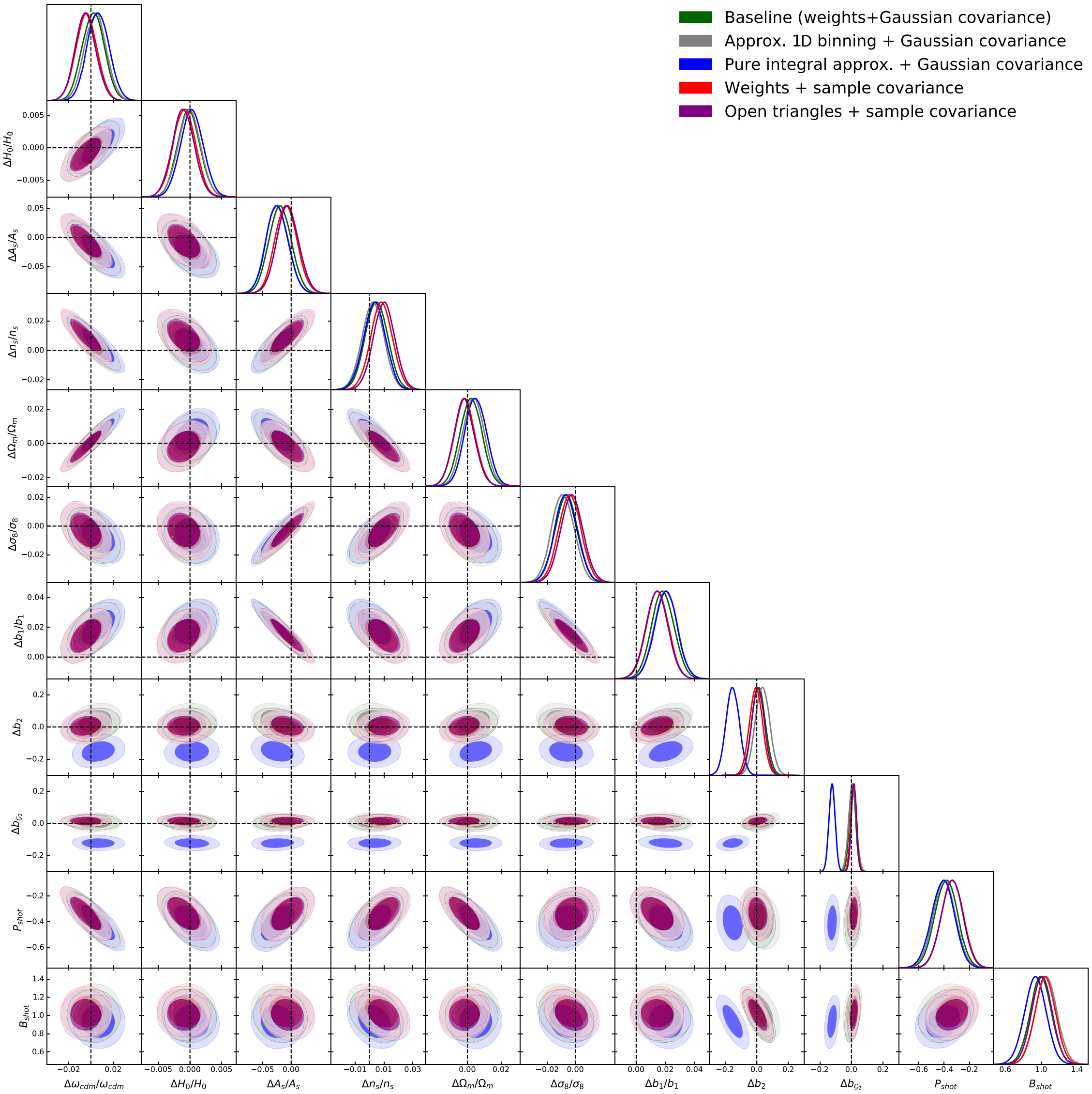

FIG. 8. Triangle plots and 1D marginalized posteriors of cosmological and nuisance parameters from the following analyses that differ by the real space bispectrum likelihood treatments: baseline (Gaussian covariance + discreteness weights), approximate 1D binning, integral approximation for binning without additional binning corrections (+Gaussian covariance for the last two cases); likelihood based on the bispectrum sample covariance (discreteness weights), and the likelihood that includes the extra open triangles (+sample covariance).

leads to significant biases in the recovery of quadratic bias parameter b_2 and $b_{\mathcal{G}_2}$.

APPENDIX B: IMPACT OF OPEN TRIANGLES

In principle, we could also include in our analysis the open triangles, i.e. the triangle bins that do not satisfy $|k_3 - k_2| < k_1 < k_3 + k_2$ at their centers. We refrained from doing so because of the reasons listed in the main text. In this Appendix we explicitly check that neglecting these triangles does not lead to any appreciable loss of information. We include these triangles in the analysis by adopting the approximate 1D binning scheme described above. We have found that the Gaussian covariance approximation is very inaccurate for them, and therefore use a diagonal sample covariance matrix in our likelihood. The sample covariance matrix approximation for "usual" closed triangle configurations is validated in the next section, showing that it leads to essentially the same results as our baseline Gaussian covariances.

The results of our analysis of the bispectrum likelihood including open triangles are shown in Fig. 8, which should be compared with the case "weights + sample covariance." We see that the posterior distribution in this case is almost identical to that of the usual sample covariance analysis without open triangles, which implies that they can safely neglected for the purposes of this paper.

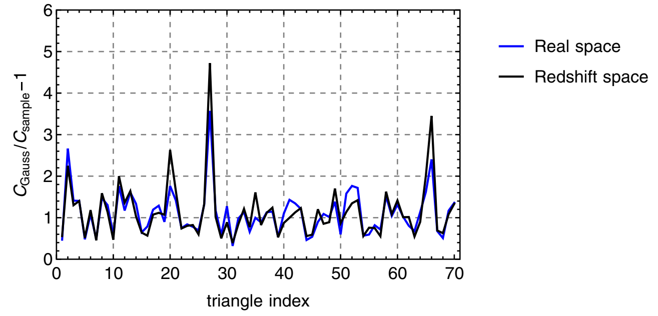

FIG. 9. Ratio of diagonal elements of the bispectrum covariance matrix computed in the Gaussian approximation and the sample covariance extracted from 10 PT challenge simulation boxes.

APPENDIX C: COVARIANCE MATRIX TESTS

To test our baseline Gaussian covariance model, in this section we run our analysis with the bispectrum likelihood based on sample covariance matrix estimators. The PT challenge suite consists of 10 boxes only, which means that the relative error on elements of the sample covariance in this case is around $10^{-1/2} \sim 30\%$. Since the sample covariance is not invertible for our baseline bispectrum data with 70 triangle bins, we will use only its diagonal part. This should still be a good approximation on large scales where the bispectrum covariance is dominated by the Gaussian diagonal contribution. The elements

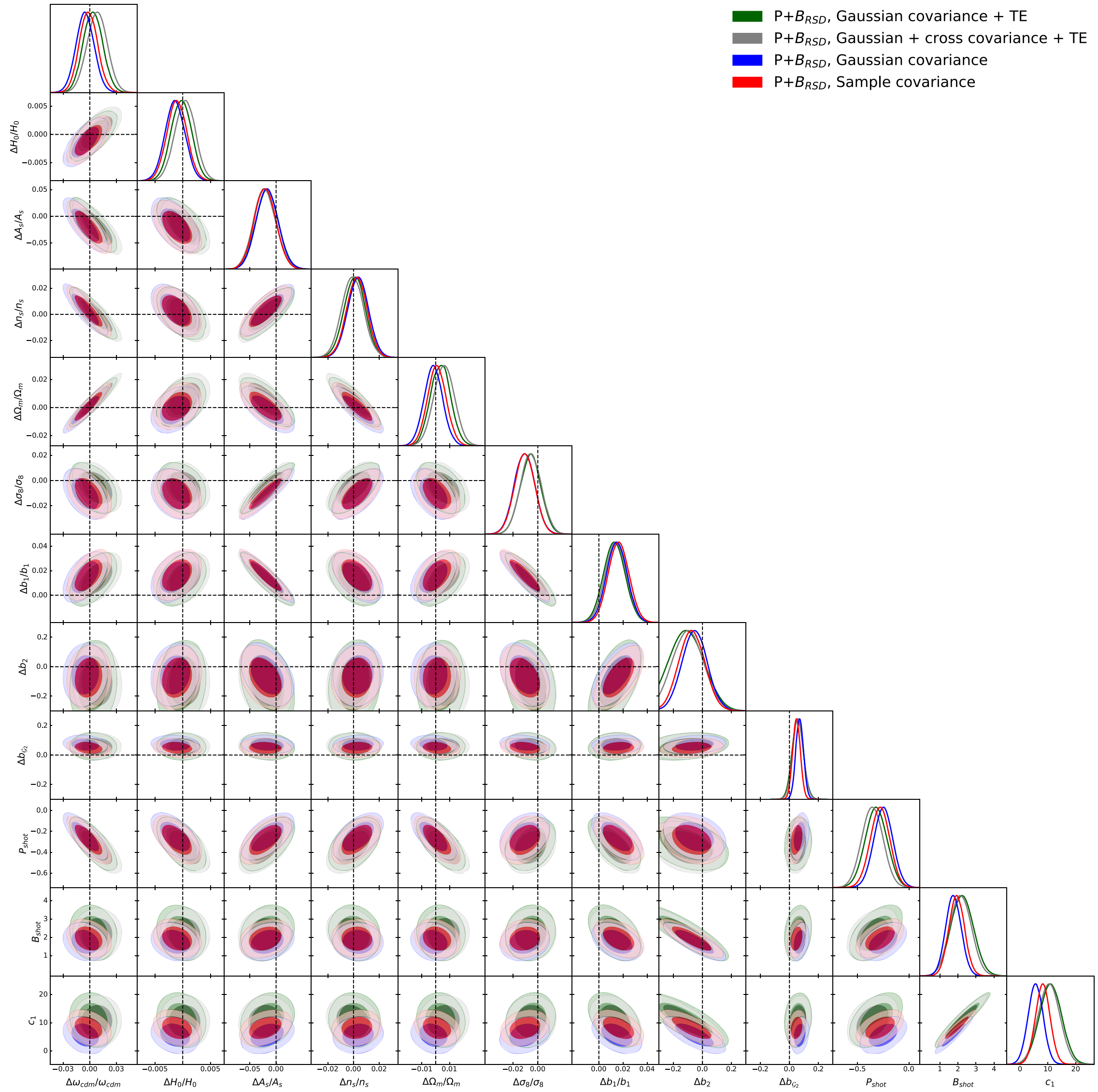

FIG. 10. Triangle plots and 1D marginalized posteriors of cosmological and nuisance parameters from the joint redshift-space power spectrum and bispectrum likelihoods built with different covariance matrices: the Gaussian covariance, the Gaussian covariance including the theoretical error (TE), the Gaussian covariance including the theoretical error and the cross-covariance between the power spectrum and bispectrum, and the bispectrum sample covariance. In all cases we have used the discreteness weights and $k_{\rm max} = 0.08\ h\,{\rm Mpc}^{-1}$ for the bispectrum likelihood.

of our sample covariance normalized to the predictions of the Gaussian approximation are shown in Fig. 9. We see that the ratio is scattered around unity with most of the points dispersed within ∼50% in accordance with the expected variance. However, we also observed several notable outliers. Nevertheless, the posterior distribution from the likelihood based on the sample covariance is almost identical to that of the baseline analysis, see Fig. 8 for the real space case and Fig. 10 for the redshift space case. We see that the main effect of the sample covariance is to shift the posterior distributions, but these shifts do not exceed 1σ, which is an expected effect of the sampling noise in the covariance [30,125].

1. Theoretical error and cross-covariance

We additionally check the stability of our results with respect to the inclusion of the theoretical error covariance to the bispectrum and the cross-covariance between the power spectrum multipoles and the bispectrum monopole.

The theoretical error covariance accounts for the imperfectness of the particular theoretical model that is used to fit the data. In the EFT approach theoretical calculations are done up to a fixed order on scales where higher order corrections are estimated to be negligible. A more systematic way to account for these corrections is to marginalize over their approximate shape dictated by the EFT power counting [4,54]. This marginalization leads to a simple change of the covariance matrix by an additive correlated contribution. We incorporate the theoretical error covariance for the bispectrum following Ref. [4]. We use the following one-loop bispectrum theoretical error kernel

$$E_B(k_1,k_2,k_3) = B_{\rm tree}(k_1,k_2,k_3,z)D_+^2(z) \times \left(\frac{k_1+k_2+k_3}{3\times 0.23\ h\,{\rm Mpc}^{-1}}\right)^{3.3}, \quad \text{(C1)}$$

whose amplitude is reduced by a factor of 3 compared to Ref. [4]. We do so because the original envelope of Ref. [4] was calibrated to one-loop calculations at $k\sim 0.2\ h\,{\rm Mpc}^{-1}$ which is larger than our baseline cut $k_{\rm max} = 0.08\ h\,{\rm Mpc}^{-1}$. We have checked that on these scales the original theory error kernel of Ref. [4] overestimates the actual size of one-loop matter bispectrum corrections, and therefore have accounted for it by multiplying this kernel by a factor 1/3. Using Eq. (C1), the theoretical error covariance can be written as

$$C_{TT'}^{B({\rm TE})} = E_B(k_1,k_2,k_3)E_B(k_1',k_2',k_3')\prod_{i=1}^{3} {\rm e}^{-\frac{(k_i-k_i')}{2\delta k^2}}, \quad \text{(C2)}$$

where the coherence scale $\delta k = 0.1\ h\,{\rm Mpc}^{-1}$ following Refs. [6,54]. The full covariance is given by

$$C_{TT'}^{B} = C_{TT'}^{B({\rm Gauss})} + C_{TT'}^{B({\rm TE})}. \quad \text{(C3)}$$

The result of our analysis of the bispectrum likelihood with the theoretical error covariance are presented in Fig. 10 and in Table III. We see the inclusion of the theoretical error covariance leads to a moderate inflation of error bars and insignificant shifts of some posteriors.

Finally, we include the cross-covariance between the power spectrum multipoles and the bispectrum monopole in our likelihood. We compute this cross-covariance in the tree-level approximation along the lines of Ref. [3], see Appendix F for more detail. The results of this analysis are displayed in the same Fig. 10 and Table III. The impact of the cross-covariance is quite marginal—the posteriors are virtually identical to those of the previous analysis which treated the bispectrum and the power spectrum uncorrelated. This is consistent with common

TABLE III. One-dimensional marginalized limits from analyses of the redshift space bispectrum monopole data at $k_{\rm max} = 0.08\ h\,{\rm Mpc}^{-1}$ with two additional ingredients: the one-loop TE bispectrum covariance (left table) and the TE bispectrum covariance plus the cross-covariance between the power spectrum multipoles and the bispectrum (right table).

TE covariance

Parameter	68% limits
$\Delta H_0/H_0$	-0.0002 ± 0.0018
$\Delta\omega_{\rm cdm}/\omega_{\rm cdm}$	0.004 ± 0.011
$\Delta A_s/A_s$	-0.017 ± 0.021
$\Delta n_s/n_s$	0.0009 ± 0.0082
$\Delta b_1/b_1$	0.0128 ± 0.0089
Δb_2	-0.11 ± 0.12
$\Delta b_{\mathcal{G}_2}$	0.058 ± 0.038
$P_{\rm shot}$	-0.32 ± 0.11
$B_{\rm shot}$	2.36 ± 0.64
c_1	11.0 ± 4.0
$\Delta\sigma_8/\sigma_8$	-0.0059 ± 0.0083
$\Delta\Omega_m/\Omega_m$	0.0035 ± 0.0072

TE + cross covariance

Parameter	68% limits
$\Delta H_0/H_0$	0.0004 ± 0.0018
$\Delta\omega_{\rm cdm}/\omega_{\rm cdm}$	0.008 ± 0.011
$\Delta A_s/A_s$	-0.021 ± 0.021
$\Delta n_s/n_s$	-0.0006 ± 0.0084
$\Delta b_1/b_1$	0.0140 ± 0.0088
Δb_2	-0.10 ± 0.11
$\Delta b_{\mathcal{G}_2}$	0.059 ± 0.037
$P_{\rm shot}$	-0.35 ± 0.10
$B_{\rm shot}$	2.15 ± 0.59
c_1	10.4 ± 3.8
$\Delta\sigma_8/\sigma_8$	-0.0056 ± 0.0084
$\Delta\Omega_m/\Omega_m$	0.0061 ± 0.0075

expectations that the cross-covariance is negligible on large scales [4,6].

All in all, the analyses that we have carried out suggest that our baseline results are stable with respect to the choice of covariance matrices.

APPENDIX D: BASELINE POWER SPECTRUM LIKELIHOOD

Our baseline power spectrum likelihood consists of two pieces:

Redshift space multipoles: $\ell = 0,\ 2,\ 4$ with $k_{\max} = 0.14\ h\,\mathrm{Mpc}^{-1}$. We build the likelihood using the Gaussian approximation for the covariance matrix of these multipole moments. In the previous work [55] we have checked that the one-loop EFT model provides an accurate and unbiased fit to the data in this range.

Transverse moment (real space) power spectrum in the range $0.14\ h\,\mathrm{Mpc}^{-1} < k < 0.4\ h\,\mathrm{Mpc}^{-1}$. We use the Gaussian covariance for real space part of the power spectrum likelihood.

Below, we present a brief overview of our theory model. We use the following deterministic part of the bias expansion (δ_g and δ are overdensity fields of galaxies and matter, respectively),

$$\delta_g = b_1\delta + \frac{b_2}{2}\delta^2 + b_{\mathcal{G}_2}\mathcal{G}_2 + b_{\Gamma_3}\Gamma_3 + R_*^2\partial_i^2\delta, \tag{D1}$$

where we introduce the Galileon operators built from the gravitational potential Φ and velocity potential Φ_v

$$\mathcal{G}_2(\Phi) = (\partial_i\partial_j\Phi)^2 - (\partial_i^2\Phi)^2, \qquad \Gamma_3 = \mathcal{G}_2(\Phi) - \mathcal{G}_2(\Phi_v). \tag{D2}$$

The higher derivative bias parameter R_*^2 is degenerate with the dark matter sound speed and the redshift-space counterterms. Thus, for convenience, we use the parametrization where each redshift space multipole has its own higher derivative counterterm,

$$P_\ell^{\mathrm{ctr}}(k) = -k^2 C_\ell \frac{2\ell+1}{2}\int_{-1}^{1} d\mu (f\mu^2)^{\frac{\ell}{2}} P_{\mathrm{tree}}^{\mathrm{IR-res}}(k,\mu)\mathcal{L}_\ell(\mu), \quad \ell = 0,2,4. \tag{D3}$$

The parameters C_0, C_2, C_4 can be easily translated into the coefficients in front of the "fundamental" line-of-sight dependent higher-derivative counterterms [44]. Note that we conservatively assume that these parameters are different from c_1, which we use in the bispectrum model. A detailed calculation of all relevant redshift-space bispectrum operators will be presented elsewhere. In addition, we include a single higher-derivative RSD counterterm

$$P_\ell^{(\hat{z}\,\vec{\nabla})^4}(k) = -k^4 b_4 \frac{2\ell+1}{2}\int_{-1}^{1} d\mu \mathcal{L}_\ell(\mu) f^4\mu^4 (b_1 + f\mu^2)^2 P_{\mathrm{tree}}^{\mathrm{IR-res}}(k,\mu), \quad \ell = 0,2,4, \tag{D4}$$

whose necessity is motivated by the analyses of the redshift-space matter power spectrum [54]. Finally, we use the following parametrization for the stochastic part of the redshift-space power spectrum,

$$P_{\mathrm{stoch}}(k,\mu) = \frac{1+P_{\mathrm{shot}}}{\bar{n}} + (a_0 + a_2\mu^2)\left(\frac{k}{0.45\ h\,\mathrm{Mpc}^{-1}}\right)^2 \frac{1}{\bar{n}}. \tag{D5}$$

Overall, our power spectrum likelihood depends on the following nuisance parameters

$$\{b_1, b_2, b_{\mathcal{G}_2}, b_{\Gamma_3}, C_0, C_2, C_4, b_4, a_0, a_2, P_{\mathrm{shot}}\}, \tag{D6}$$

for which we assume the following physically motivated priors [44,53,54,77]:

$$\begin{gathered} b_1 \in (1,4), \qquad b_2 \sim \mathcal{N}(0,1^2), \qquad b_{\mathcal{G}_2} \sim \mathcal{N}(0,1^2), \qquad b_{\Gamma_3} \sim \mathcal{N}\left(\frac{23}{42}(b_1^{\mathrm{fid}}-1), 1^2\right), \\ \frac{C_0}{(h^{-1}\,\mathrm{Mpc})^2} \sim \mathcal{N}(4,10^2), \qquad \frac{C_2}{(h^{-1}\,\mathrm{Mpc})^2} \sim \mathcal{N}(20,20^2), \qquad \frac{C_4}{(h^{-1}\,\mathrm{Mpc})^2} \sim \mathcal{N}(-10,20^2), \\ \frac{b_4}{(h^{-1}\,\mathrm{Mpc})^4} \sim \mathcal{N}(500,500^2), \qquad a_0 \sim \mathcal{N}(0,1^2), \qquad a_2 \sim \mathcal{N}(0,1^2), \qquad P_{\mathrm{shot}} \sim \mathcal{N}(0,1^2). \end{gathered} \tag{D7}$$

APPENDIX E: REAL SPACE POWER SPECTRUM + BISPECTRUM ANALYSIS

In this appendix we study the information content of clustering statistics purely in real space. Similar analyses have done before, see for instance [11–13]. We analyze the real space galaxy power spectrum of PT challenge simulation at $k_{\max} = 0.2\ h\,\mathrm{Mpc}^{-1}$ and the real space bispectrum at $k_{\max} = 0.08\ h\,\mathrm{Mpc}^{-1}$. The real space power spectrum case is very different from the redshift space one. In the absence of RSD the degeneracy between the linear galaxy bias b_1 and clustering amplitude σ_8 is largely unbroken. Moreover, the real space case does not capture the distance information, which should result in larger error bars on H_0.

Our results are shown in Fig. 11 and in Table VI. The real space power spectrum data $P_{\mathrm{gg,real}}$ is much less constraining than the dataset $[P_0, P_2, P_4, Q_0]$ that we are using in our baseline redshift space power spectrum analysis. In particular, the constraints on $\omega_{\mathrm{cdm}}, n_s$, and H_0 are a few times weaker, and the limit on σ_8 is weaker by an order of magnitude. We can also see that the cosmological parameters' posteriors from the bispectrum alone are comparable to the power spectrum ones. When we combine the two statistics the improvement is quite significant, e.g. the limit on σ_8 improves by a factor of four, the limit on H_0 by 30%.

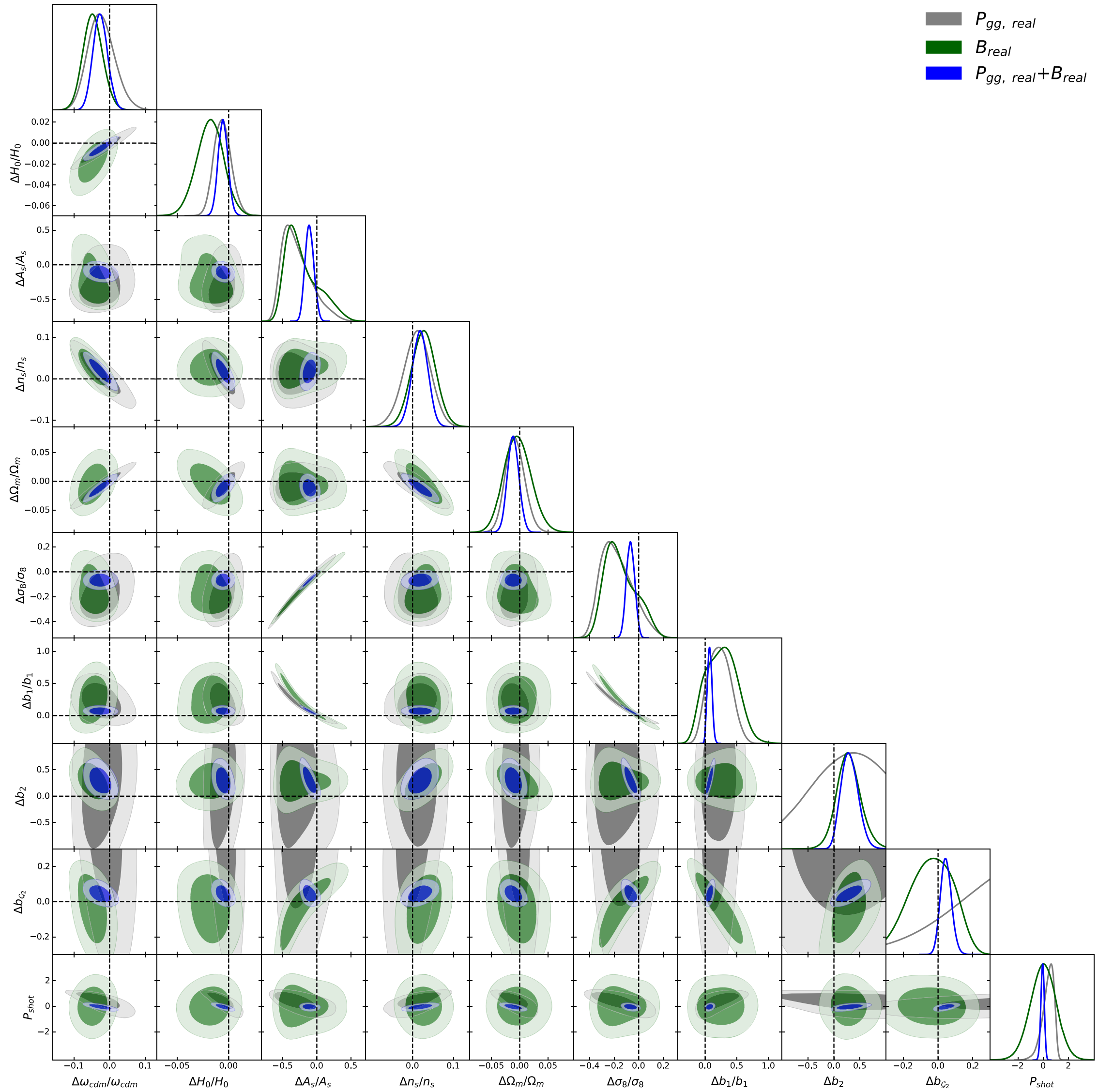

FIG. 11. Triangle plots and 1D marginalized posteriors of cosmological and nuisance parameters from the real space power spectra and bispectra data of the PT challenge simulation. For compactness, only linear and quadratic bias parameters are shown.

TABLE IV. One-dimensional marginalized limits from analyses of the real space power spectrum at $k_{\max} = 0.20\ h\,\mathrm{Mpc}^{-1}$ and the real space bispectrum at $k_{\max} = 0.08\ h\,\mathrm{Mpc}^{-1}$. For compactness, only linear and quadratic bias parameters are shown.

$P_{\mathrm{gg,real}}$, real space	
Parameter	68% limits
$\Delta H_0/H_0$	$-0.0058^{+0.0076}_{-0.0089}$
$\Delta\omega_{\mathrm{cdm}}/\omega_{\mathrm{cdm}}$	$-0.023^{+0.033}_{-0.040}$
$\Delta A_s/A_s$	$-0.29^{+0.13}_{-0.26}$
$\Delta n_s/n_s$	0.011 ± 0.033
$\Delta b_1/b_1$	$0.22^{+0.17}_{-0.19}$
Δb_2	0.43 ± 0.91
$\Delta b_{\mathcal{G}_2}$	$0.71^{+0.43}_{-0.55}$
P_{shot}	$0.38^{+0.57}_{-0.29}$
$\Delta\sigma_8/\sigma_8$	$-0.177^{+0.097}_{-0.16}$
$\Delta\Omega_m/\Omega_m$	$-0.008^{+0.015}_{-0.018}$

B_{real}, real space	
Parameter	68% limits
$\Delta H_0/H_0$	-0.018 ± 0.013
$\Delta\omega_{\mathrm{cdm}}/\omega_{\mathrm{cdm}}$	-0.047 ± 0.028
$\Delta A_s/A_s$	$-0.22^{+0.13}_{-0.31}$
$\Delta n_s/n_s$	0.027 ± 0.029
$\Delta b_1/b_1$	0.25 ± 0.24
Δb_2	$0.29^{+0.21}_{-0.24}$
$\Delta b_{\mathcal{G}_2}$	$-0.04^{+0.15}_{-0.11}$
P_{shot}	0.0 ± 1.0
B_{shot}	0.87 ± 0.32
$\Delta\sigma_8/\sigma_8$	$-0.148^{+0.091}_{-0.16}$
$\Delta\Omega_m/\Omega_m$	$-0.004^{+0.022}_{-0.025}$

$P_{\mathrm{gg,real}} + B_{\mathrm{real}}$, real space	
Parameter	68% limits
$\Delta H_0/H_0$	-0.0054 ± 0.0047
$\Delta\omega_{\mathrm{cdm}}/\omega_{\mathrm{cdm}}$	-0.026 ± 0.020
$\Delta A_s/A_s$	$-0.107^{+0.060}_{-0.068}$
$\Delta n_s/n_s$	0.018 ± 0.019
$\Delta b_1/b_1$	0.071 ± 0.036
Δb_2	$0.30^{+0.15}_{-0.18}$
$\Delta b_{\mathcal{G}_2}$	$0.046^{+0.029}_{-0.034}$
P_{shot}	-0.05 ± 0.14
B_{shot}	0.96 ± 0.18
$\Delta\sigma_8/\sigma_8$	-0.066 ± 0.033
$\Delta\Omega_m/\Omega_m$	-0.011 ± 0.010

APPENDIX F: POWER SPECTRUM AND BISPECTRUM COVARIANCES IN PERTURBATION THEORY

In this appendix we calculate tree-level covariance matrices for the power spectrum and bispectrum. Let us start with the real-space estimators for the density power spectrum and bispectrum in the narrow bin approximation $\Delta k \ll k$ [23]

$$\begin{aligned}
\hat{P}(k_i) &= \int_{q\in k_i\mathrm{shell}} \frac{d^3q}{(2\pi)^3\mathcal{N}_k}\delta(-\mathbf{q})\delta(\mathbf{q}),\\
\mathcal{N}_k &= 4\pi k^2\Delta k\frac{V}{(2\pi)^3}.\\
\hat{B}(k_1,k_2,k_3) &= \prod_{i=1}^{3}\int_{k_i}\frac{d^3q_i}{(2\pi)^3}\frac{(2\pi)^3\delta^{(3)}(\mathbf{q}_{123})}{N_T^{123}}\delta(\mathbf{q}_1)\delta(\mathbf{q}_2)\delta(\mathbf{q}_3),\\
N_T^{123} &= 8\pi^2 k_1k_2k_3\Delta k^3\frac{V^2}{(2\pi)^6},
\end{aligned} \tag{F1}$$

Using the formulas from [102],

$$\begin{aligned}
&\int r^2 dr j_0(k_1r)j_0(k_2r)j_0(k_3r) = \frac{\pi}{4},\\
&\int_{k_1}\int_{k_2}\int_{k_3}[dq]^3(2\pi)^3\delta^{(3)}(\mathbf{q}_{123}) = k_1k_2k_3\Delta k^3\frac{(4\pi)^4}{(2\pi)^9}\frac{\pi}{4},\\
&\delta_D^{(3)}(\mathbf{k}_1+\mathbf{k}_2+\mathbf{k}_3) = \frac{1}{k_1k_2k_3}\delta_D^{(1)}\left(\cos(\mathbf{k}_1,\mathbf{k}_2) - \frac{k_3^2-k_1^2-k_1^2}{2k_1k_2}\right)\delta_D^{(2)}(\hat{\mathbf{k}}_3 - (\hat{\mathbf{k}}_1+\hat{\mathbf{k}}_2)),
\end{aligned} \tag{F2}$$

we can compute the autocovariances of the estimators (F1),

$$\begin{aligned}
C_{k_ik_j} &= \frac{2}{\mathcal{N}_{k_i}}\delta_{ij}P^2(k_i),\\
C_{TT'} &= \frac{(2\pi)^3\pi s_{123}}{k_1k_2k_3\Delta k^3 V}\delta_{TT'}\prod_{i=1}^{3}P(k_i),
\end{aligned} \tag{F3}$$

where $s_{123} = 6$, 2, or 1 for equilateral, isosceles, and general triangles. The cross-covariance $\langle P(k')B(k_1,k_2,k_3)\rangle$ is given by

$$C_{k'_iT} = \frac{2(2\pi)^3}{\mathcal{N}_{k'_i}}(\delta_{ij_1}P(k'_i)B(k_{j_1},k_{j_2},k_{j_3}) + \text{cycl.}). \tag{F4}$$

It is straightforward to generalize these calculations to power spectrum multipole ℓ and the redshift-space bispectrum multipole ℓ',

$$\begin{aligned}
\hat{P}_\ell(k_i) &= \int_{q\in k_i\ \mathrm{shell}}\frac{d^3q}{(2\pi)^3\mathcal{N}_k}\delta_0(-\mathbf{q})\delta_0(\mathbf{q})(2\ell+1)\times\mathcal{L}_\ell(\hat{\mathbf{z}}\cdot\hat{\mathbf{q}}),\\
\hat{B}_{\ell'}(k_1,k_2,k_3) &= (2\ell'+1)\prod_{i=1}^{3}\int_{k_i}\frac{d^3q_i}{(2\pi)^3}\frac{(2\pi)^3\delta_D^{(3)}(\mathbf{q}_{123})}{N_T^{123}}\times\delta(\mathbf{q}_1)\delta(\mathbf{q}_2)\delta(\mathbf{q}_3)\mathcal{L}_{\ell'}(\hat{\mathbf{z}}\cdot\hat{\mathbf{q}}_1),
\end{aligned} \tag{F5}$$

where $\delta_0(\mathbf{k}) = \delta(\mathbf{k})(1+\beta\mu^2)$ in the linear approximation [126], $\beta \equiv f/b_1$. In particular, this implies that the continuous part of the angle-averaged bispectrum autocovariance would be modulated in redshift space by a form factor

$$\int \frac{d\phi}{2\pi}\int_0^1 d\mu (1+\beta\mu^2)^2(1+\beta\mu_2(\mu,\phi)^2)^2(1+\beta\mu_3(\mu,\phi)^2)^2. \tag{F6}$$

Similarly, the cross-correlation between P_ℓ and B_0 is given by

$$\begin{aligned}\langle P_\ell(k)B_0(k_1,k_2,k_3)\rangle = \frac{2(2\pi)^3(2\ell+1)}{\mathcal{N}_k}\Big(\delta_{kk_1}P(k)\int\frac{d\phi}{2\pi}\\ \times\int_0^1 d\mu(1+\beta\mu^2)^2\mathcal{L}_\ell(\mu)\\ \times B(\mathbf{k},\mathbf{k}_2,\mathbf{k}_3) + \text{cycl.}\Big).\end{aligned} \tag{F7}$$

APPENDIX G: GAUSSIAN FINGERS-OF-GOD EXPONENT DERIVATION

In this section we revisit the derivation of the Gaussian FOG exponent that is often used in the literature to motivate some phenomenological models for FOG, see e.g. [19]. Reference [54] has explicitly shown that this model completely fails to capture the behavior seen in high quality dark matter redshift space simulations. Nevertheless, it would be of some interest to see when the Gaussian FOG model breaks down at the mathematical level. Let us consider the redshift space mapping,

$$\delta^{(z)}(\mathbf{k}) = \int d^3x e^{i\mathbf{k}\mathbf{x}+i\mathcal{H}^{-1}k_z v_z(\mathbf{x})}(\delta(\mathbf{x})+1) - (2\pi)^3\delta_D^{(3)}(\mathbf{k}). \tag{G1}$$

Now we split the velocity field into the long and short wavelength components,

$$v_i = v_i^L + v_i^S, \tag{G2}$$

where v^L is correlated with the density field on large scales and v^S is the short-scale contribution generated by the nonperturbative effects such as virialization. A common assumption is that this part is fully uncorrelated with the perturbative long wavelength density field. Taylor-expanding the exponent over its perturbative part we have

$$\delta^{(z)}(\mathbf{k}) = \int d^3x e^{i\mathbf{k}\mathbf{x}+i\mathcal{H}^{-1}k_z v_z^S(\mathbf{x})}(\delta(\mathbf{x}) + i\mathcal{H}^{-1}k_z v_z^L(\mathbf{x})), \tag{G3}$$

where we have neglected terms which have support only around $\mathbf{k}=0$. In what follows we restrict ourselves to the tree-level order for the perturbative part, in which case the velocity field can be expressed as

$$v_i^L = -f\mathcal{H}\frac{\partial_i\delta_m^L}{\Delta} \Rightarrow i\mathcal{H}^{-1}k_z v_i^L(\mathbf{k}) = f\mu^2\delta_m^L(\mathbf{k}). \tag{G4}$$

In order to reproduce the Gaussian FOG exponent, we need to assume the short scale velocity field is Gaussian distributed, and its two point correlation function has a finite support on short scales,

$$\langle v_i(\mathbf{x})v_j(\mathbf{x}')\rangle = \delta_{ij}\mathcal{H}^2\sigma_v^2 \quad \text{for } \mathbf{x}=\mathbf{x}' \quad \text{and} \quad 0 \text{ otherwise}. \tag{G5}$$

Clearly, this assumption cannot be justified within the EFT approach, which requires that the short-scale averages should depend on all possible operators involving low-energy degrees of freedom compatible with IR symmetries of large-scale structure [42]. Nevertheless, if we proceed using the cumulant expansion theorem

$$\langle\exp\{iX\}\rangle = \exp\left\{\sum_{N=1}^{\infty}\frac{i^N}{N!}\langle X^N\rangle_c\right\}, \tag{G6}$$

we find the power spectrum in redshift space given by

$$\langle\delta^{(z)}(\mathbf{k})\delta^{(z)}(\mathbf{k}')\rangle = (2\pi)^3\delta_D^{(3)}(\mathbf{k}+\mathbf{k}')e^{-\sigma_v^2\mu^2k^2}P_{\text{Kaiser}}(k), \tag{G7}$$

where

$$P_{\text{Kaiser}}(k) = (b_1+f\mu^2)^2P(k) + \frac{1}{\bar{n}}. \tag{G8}$$

For the redshift space bispectrum we have

$$\begin{aligned}&\langle\delta^{(z)}(\mathbf{k}_1)\delta^{(z)}(\mathbf{k}_2)\delta^{(z)}(\mathbf{k}_3)\rangle\\ &\quad = (2\pi)^3\delta_D^{(3)}(\mathbf{k}_{123})e^{-\frac{\sigma_v^2}{2}\sum_{a=1}^3\mu_a^2k_a^2}B_{\text{tree}}(\mathbf{k}_1,\mathbf{k}_2,\mathbf{k}_3),\end{aligned} \tag{G9}$$

which would formally coincide with the leading order EFT expression used in this work if we Taylor expand the damping exponent and identify

$$c_1 = \frac{(k_{\text{NL}}^r)^2}{2}\sigma_v^2 b_1, \qquad c_2 = \frac{(k_{\text{NL}}^r)^2}{2}\sigma_v^2 f. \tag{G10}$$

---

[1] P. J. E. Peebles, *The Large-Scale Structure of the Universe* (Princeton University Press, 1980), ISBN: 978-0-691-08240-0, https://ui.adsabs.harvard.edu/abs/1980lssu.book.....P/abstract.

[2] R. Scoccimarro, The bispectrum: From theory to observations, Astrophys. J. **544**, 597 (2000).

[3] E. Sefusatti, M. Crocce, S. Pueblas, and R. Scoccimarro, Cosmology and the Bispectrum, Phys. Rev. D **74**, 023522 (2006).

[4] T. Baldauf, M. Mirbabayi, M. Simonović, and M. Zaldarriaga, LSS constraints with controlled theoretical uncertainties, arXiv:1602.00674.

[5] V. Yankelevich and C. Porciani, Cosmological information in the redshift-space bispectrum, Mon. Not. R. Astron. Soc. **483**, 2078 (2019).

[6] A. Chudaykin and M. M. Ivanov, Measuring neutrino masses with large-scale structure: Euclid forecast with controlled theoretical error, J. Cosmol. Astropart. Phys. 11 (2019) 034.

[7] C. Hahn, F. Villaescusa-Navarro, E. Castorina, and R. Scoccimarro, Constraining M_ν with the bispectrum. Part I. Breaking parameter degeneracies, J. Cosmol. Astropart. Phys. 03 (2020) 040.

[8] C. Hahn and F. Villaescusa-Navarro, Constraining M_ν with the bispectrum. Part II. The information content of the galaxy bispectrum monopole, J. Cosmol. Astropart. Phys. 04 (2021) 029.

[9] Y. Welling, D. van der Woude, and E. Pajer, Lifting primordial non-gaussianity above the noise, J. Cosmol. Astropart. Phys. 08 (2016) 044.

[10] A. Moradinezhad Dizgah, M. Biagetti, E. Sefusatti, V. Desjacques, and J. Noreña, Primordial non-gaussianity from biased tracers: Likelihood analysis of real-space power spectrum and bispectrum, J. Cosmol. Astropart. Phys. 05 (2021) 015.

[11] A. Oddo, E. Sefusatti, C. Porciani, P. Monaco, and A. G. Sánchez, Toward a robust inference method for the galaxy bispectrum: Likelihood function and model selection, J. Cosmol. Astropart. Phys. 03 (2020) 056.

[12] A. Eggemeier, R. Scoccimarro, R. E. Smith, M. Crocce, A. Pezzotta, and A. G. Sánchez, Testing one-loop galaxy bias: Joint analysis of power spectrum and bispectrum, Phys. Rev. D **103**, 123550 (2021).

[13] A. Oddo, F. Rizzo, E. Sefusatti, C. Porciani, and P. Monaco, Cosmological parameters from the likelihood analysis of the galaxy power spectrum and bispectrum in real space, J. Cosmol. Astropart. Phys. 11 (2021) 038.

[14] P. J. E. Peebles and E. J. Groth, Statistical analysis of catalogs of extragalactic objects. V. Three-point correlation function for the galaxy distribution in the Zwicky catalog, Astrophys. J. **196**, 1 (1975).

[15] E. J. Groth and P. J. E. Peebles, Statistical analysis of catalogs of extragalactic objects. VII. Two- and three-point correlation functions for the high-resolution Shane-Wirtanen catalog of galaxies, Astrophys. J. **217**, 385 (1977).

[16] R. Scoccimarro, H. A. Feldman, J. N. Fry, and J. A. Frieman, The bispectrum of IRAS redshift catalogs, Astrophys. J. **546**, 652 (2001).

[17] H. A. Feldman, J. A. Frieman, J. N. Fry, and R. Scoccimarro, Constraints on Galaxy Bias, Matter Density, and Primordial Non-Gausianity from the PSCz Galaxy Redshift Survey, Phys. Rev. Lett. **86**, 1434 (2001).

[18] F. A. Marin *et al.* (WiggleZ Collaboration), The WiggleZ Dark Energy Survey: Constraining galaxy bias and cosmic growth with 3-point correlation functions, Mon. Not. R. Astron. Soc. **432**, 2654 (2013).

[19] H. Gil-Marn, J. Norea, L. Verde, W. J. Percival, C. Wagner, M. Manera, and D. P. Schneider, The power spectrum and bispectrum of SDSS DR11 BOSS galaxies I. Bias and gravity, Mon. Not. R. Astron. Soc. **451**, 539 (2015).

[20] H. Gil-Marn, L. Verde, J. Norea, A. J. Cuesta, L. Samushia, W. J. Percival, C. Wagner, M. Manera, and D. P. Schneider, The power spectrum and bispectrum of SDSS DR11 BOSS galaxies II. Cosmological interpretation, Mon. Not. R. Astron. Soc. **452**, 1914 (2015).

[21] H. Gil-Marn, W. J. Percival, L. Verde, J. R. Brownstein, C.-H. Chuang, F.-S. Kitaura, S. A. Rodríguez-Torres, and M. D. Olmstead, The clustering of galaxies in the SDSS-III Baryon Oscillation Spectroscopic Survey: RSD measurement from the power spectrum and bispectrum of the DR12 BOSS galaxies, Mon. Not. R. Astron. Soc. **465**, 1757 (2017).

[22] Z. Slepian *et al.*, The large-scale three-point correlation function of the SDSS BOSS DR12 CMASS galaxies, Mon. Not. R. Astron. Soc. **468**, 1070 (2017).

[23] R. Scoccimarro, Fast estimators for redshift-space clustering, Phys. Rev. D **92**, 083532 (2015).

[24] O. H. E. Philcox and D. J. Eisenstein, Computing the small-scale galaxy power spectrum and bispectrum in configuration-space, Mon. Not. R. Astron. Soc. **492**, 1214 (2020).

[25] O. H. E. Philcox and D. J. Eisenstein, Estimating covariance matrices for two- and three-point correlation function moments in arbitrary survey geometries, Mon. Not. R. Astron. Soc. **490**, 5931 (2019).

[26] O. H. E. Philcox, A faster Fourier transform? Computing small-scale power spectra and bispectra for cosmological simulations in $\mathcal{O}(N^2)$ time, Mon. Not. R. Astron. Soc. **501**, 4004 (2021).

[27] O. H. E. Philcox, Z. Slepian, J. Hou, C. Warner, R. N. Cahn, and D. J. Eisenstein, ENCORE: Estimating galaxy N-point correlation functions in $\mathcal{O}(N_{\mathrm{g}}^2)$ time, Mon. Not. R. Astron. Soc. **509**, 2457 (2022).

[28] E. Gaztanaga and R. Scoccimarro, The 3-point function in large scale structure: Redshift distortions and galaxy bias, Mon. Not. R. Astron. Soc. **361**, 824 (2005).

[29] D. Gualdi, H. Gil-Marín, R. L. Schuhmann, M. Manera, B. Joachimi, and O. Lahav, Enhancing BOSS bispectrum cosmological constraints with maximal compression, Mon. Not. R. Astron. Soc. **484**, 3713 (2019).

[30] O. H. E. Philcox, M. M. Ivanov, M. Zaldarriaga, M. Simonovic, and M. Schmittfull, Fewer mocks and less noise: Reducing the dimensionality of cosmological observables with subspace projections, Phys. Rev. D **103**, 043508 (2021).

[31] F.-S. Kitaura *et al.*, The clustering of galaxies in the SDSS-III baryon oscillation spectroscopic survey: Mock galaxy

catalogues for the BOSS final data release, Mon. Not. R. Astron. Soc. **456**, 4156 (2016).

[32] F.-S. Kitaura, H. Gil-Marn, C. Scoccola, C.-H. Chuang, V. Mller, G. Yepes, and F. Prada, Constraining the halo bispectrum in real and redshift space from perturbation theory and non-linear stochastic bias, Mon. Not. R. Astron. Soc. **450**, 1836 (2015).

[33] R. Takahashi, T. Nishimichi, T. Namikawa, A. Taruya, I. Kayo, K. Osato, Y. Kobayashi, and M. Shirasaki, Fitting the nonlinear matter bispectrum by the halofit approach, Astrophys. J. **895**, 113 (2020).

[34] K. Heitmann, D. Higdon, M. White, S. Habib, B. J. Williams, and C. Wagner, The coyote universe II: Cosmological models and precision emulation of the nonlinear matter power spectrum, Astrophys. J. **705**, 156 (2009).

[35] T. Nishimichi, M. Takada, R. Takahashi, K. Osato, M. Shirasaki, T. Oogi *et al.*, Dark quest. I. Fast and accurate emulation of halo clustering statistics and its application to galaxy clustering, Astrophys. J. **884**, 29 (2019).

[36] Y. Kobayashi, T. Nishimichi, M. Takada, R. Takahashi, and K. Osato, Accurate emulator for the redshift-space power spectrum of dark matter halos and its application to galaxy power spectrum, Phys. Rev. D **102**, 063504 (2020).

[37] A. Schneider, R. Teyssier, D. Potter, J. Stadel, J. Onions, D. S. Reed, R. E. Smith, V. Springel, F. R. Pearce, and R. Scoccimarro, Matter power spectrum and the challenge of percent accuracy, J. Cosmol. Astropart. Phys. 04 (2016) 047.

[38] J. N. Fry, The Galaxy correlation hierarchy in perturbation theory, Astrophys. J. **279**, 499 (1984).

[39] R. Scoccimarro and J. Frieman, Loop corrections in nonlinear cosmological perturbation theory, Astrophys. J. Suppl. Ser. **105**, 37 (1996).

[40] R. Scoccimarro, S. Colombi, J. N. Fry, J. A. Frieman, E. Hivon, and A. Melott, Nonlinear evolution of the bispectrum of cosmological perturbations, Astrophys. J. **496**, 586 (1998).

[41] R. Scoccimarro, H. M. P. Couchman, and J. A. Frieman, The bispectrum as a signature of gravitational instability in redshift-space, Astrophys. J. **517**, 531 (1999).

[42] D. Baumann, A. Nicolis, L. Senatore, and M. Zaldarriaga, Cosmological non-linearities as an effective fluid, J. Cosmol. Astropart. Phys. 07 (2012) 051.

[43] J. J. M. Carrasco, M. P. Hertzberg, and L. Senatore, The effective field theory of cosmological large scale structures, J. High Energy Phys. 09 (2012) 082.

[44] A. Chudaykin, M. M. Ivanov, O. H. E. Philcox, and M. Simonović, Nonlinear perturbation theory extension of the Boltzmann code CLASS, Phys. Rev. D **102**, 063533 (2020).

[45] G. D'Amico, L. Senatore, and P. Zhang, Limits on *w*CDM from the EFTofLSS with the PyBird code, J. Cosmol. Astropart. Phys. 01 (2021) 006.

[46] S.-F. Chen, Z. Vlah, E. Castorina, and M. White, Redshift-space distortions in lagrangian perturbation theory, J. Cosmol. Astropart. Phys. 03 (2021) 100.

[47] S. Alam *et al.* (BOSS Collaboration), The clustering of galaxies in the completed SDSS-III Baryon Oscillation Spectroscopic Survey: Cosmological analysis of the DR12 galaxy sample, Mon. Not. R. Astron. Soc. **470**, 2617 (2017).

[48] M. M. Ivanov, M. Simonović, and M. Zaldarriaga, Cosmological parameters from the BOSS galaxy power spectrum, J. Cosmol. Astropart. Phys. 05 (2020) 042.

[49] G. D'Amico, J. Gleyzes, N. Kokron, D. Markovic, L. Senatore, P. Zhang, F. Beutler, and H. Gil-Marín, The cosmological analysis of the SDSS/BOSS data from the effective field theory of large-scale structure, J. Cosmol. Astropart. Phys. 05 (2020) 005.

[50] M. M. Ivanov, M. Simonović, and M. Zaldarriaga, Cosmological parameters and neutrino masses from the final Planck and full-shape BOSS data, Phys. Rev. D **101**, 083504 (2020).

[51] M. M. Ivanov, E. McDonough, J. C. Hill, M. Simonović, M. W. Toomey, S. Alexander, and M. Zaldarriaga, Constraining early dark energy with large-scale structure, Phys. Rev. D **102**, 103502 (2020).

[52] G. D'Amico, L. Senatore, P. Zhang, and H. Zheng, The Hubble tension in light of the full-shape analysis of large-scale structure data, J. Cosmol. Astropart. Phys. 05 (2021) 072.

[53] A. Chudaykin, K. Dolgikh, and M. M. Ivanov, Constraints on the curvature of the Universe and dynamical dark energy from the full-shape and BAO data, Phys. Rev. D **103**, 023507 (2021).

[54] A. Chudaykin, M. M. Ivanov, and M. Simonović, Optimizing large-scale structure data analysis with the theoretical error likelihood, Phys. Rev. D **103**, 043525 (2021).

[55] T. Nishimichi, G. D'Amico, M. M. Ivanov, L. Senatore, M. Simonović, M. Takada, M. Zaldarriaga, and P. Zhang, Blinded challenge for precision cosmology with large-scale structure: Results from effective field theory for the redshift-space galaxy power spectrum, Phys. Rev. D **102**, 123541 (2020).

[56] P. Valageas and T. Nishimichi, Combining perturbation theories with halo models for the matter bispectrum, Astron. Astrophys. **532**, A4 (2011).

[57] R. E. Angulo, S. Foreman, M. Schmittfull, and L. Senatore, The one-loop matter bispectrum in the effective field theory of large scale structures, J. Cosmol. Astropart. Phys. 10 (2015) 039.

[58] T. Baldauf, L. Mercolli, M. Mirbabayi, and E. Pajer, The bispectrum in the effective field theory of large scale structure, J. Cosmol. Astropart. Phys. 05 (2015) 007.

[59] D. Bertolini, K. Schutz, M. P. Solon, and K. M. Zurek, The trispectrum in the effective field theory of large scale structure, J. Cosmol. Astropart. Phys. 06 (2016) 052.

[60] A. Eggemeier, R. Scoccimarro, and R. E. Smith, Bias loop corrections to the galaxy bispectrum, Phys. Rev. D **99**, 123514 (2019).

[61] A. Taruya, T. Nishimichi, and D. Jeong, Grid-based calculation for perturbation theory of large-scale structure, Phys. Rev. D **98**, 103532 (2018).

[62] K. Osato, T. Nishimichi, A. Taruya, and F. Bernardeau, Implementing spectra response function approaches for fast calculation of power spectra and bispectra, Phys. Rev. D **104**, 103501 (2021).

[63] D. Alkhanishvili, C. Porciani, E. Sefusatti, M. Biagetti, A. Lazanu, A. Oddo *et al.*, The reach of next-to-leading-order

perturbation theory for the matter bispectrum, arXiv:2107.08054.

[64] L. Senatore and M. Zaldarriaga, Redshift space distortions in the effective field theory of large scale structures, arXiv:1409.1225.

[65] M. Lewandowski, L. Senatore, F. Prada, C. Zhao, and C.-H. Chuang, EFT of large scale structures in redshift space, Phys. Rev. D **97**, 063526 (2018).

[66] A. Perko, L. Senatore, E. Jennings, and R. H. Wechsler, Biased tracers in redshift space in the EFT of large-scale structure, arXiv:1610.09321.

[67] L. Senatore, Bias in the effective field theory of large scale structures, J. Cosmol. Astropart. Phys. 11 (2015) 007.

[68] R. Angulo, M. Fasiello, L. Senatore, and Z. Vlah, On the statistics of biased tracers in the effective field theory of large scale structures, J. Cosmol. Astropart. Phys. 09 (2015) 029.

[69] V. Assassi, D. Baumann, D. Green, and M. Zaldarriaga, Renormalized halo bias, J. Cosmol. Astropart. Phys. 08 (2014) 056.

[70] M. Mirbabayi, F. Schmidt, and M. Zaldarriaga, Biased tracers and time evolution, J. Cosmol. Astropart. Phys. 07 (2015) 030.

[71] V. Desjacques, D. Jeong, and F. Schmidt, Large-scale galaxy bias, Phys. Rep. **733**, 1 (2018).

[72] V. Desjacques, D. Jeong, and F. Schmidt, The galaxy power spectrum and bispectrum in redshift space, J. Cosmol. Astropart. Phys. 12 (2018) 035.

[73] D. Blas, M. Garny, M. M. Ivanov, and S. Sibiryakov, Time-sliced perturbation theory II: Baryon acoustic oscillations and infrared resummation, J. Cosmol. Astropart. Phys. 07 (2016) 028.

[74] M. M. Ivanov and S. Sibiryakov, Infrared resummation for biased tracers in redshift space, J. Cosmol. Astropart. Phys. 07 (2018) 053.

[75] A. Taruya, T. Nishimichi, and D. Jeong, Grid-based calculations of redshift-space matter fluctuations from perturbation theory: UV sensitivity and convergence at the field level, arXiv:2109.06734.

[76] C. Alcock and B. Paczynski, An evolution free test for non-zero cosmological constant, Nature (London) **281**, 358 (1979).

[77] M. M. Ivanov, O. H. E. Philcox, M. Simonović, M. Zaldarriaga, T. Nishimichi, and M. Takada, Cosmological constraints without fingers of God, arXiv:2110.00006.

[78] A. J. S. Hamilton and M. Tegmark, The Real space power spectrum of the PSCz survey from 0.01 to 300 $h\,\mathrm{Mpc}^{-1}$, Mon. Not. R. Astron. Soc. **330**, 506 (2002).

[79] M. Tegmark *et al.* (SDSS Collaboration), The 3-D power spectrum of galaxies from the SDSS, Astrophys. J. **606**, 702 (2004).

[80] R. Scoccimarro, Redshift-space distortions, pairwise velocities and nonlinearities, Phys. Rev. D **70**, 083007 (2004).

[81] F. Bernardeau, S. Colombi, E. Gaztanaga, and R. Scoccimarro, Large scale structure of the universe and cosmological perturbation theory, Phys. Rep. **367**, 1 (2002).

[82] M. Schmittfull, T. Baldauf, and U. Seljak, Near optimal bispectrum estimators for large-scale structure, Phys. Rev. D **91**, 043530 (2015).

[83] R. Casas-Miranda, H. J. Mo, R. K. Sheth, and G. Boerner, On the distribution of haloes, galaxies and mass, Mon. Not. R. Astron. Soc. **333**, 730 (2002).

[84] T. Baldauf, U. Seljak, R. E. Smith, N. Hamaus, and V. Desjacques, Halo stochasticity from exclusion and nonlinear clustering, Phys. Rev. D **88**, 083507 (2013).

[85] T. Baldauf, S. Codis, V. Desjacques, and C. Pichon, Peak exclusion, stochasticity and convergence of perturbative bias expansions in $1+1$ gravity, Mon. Not. R. Astron. Soc. **456**, 3985 (2016).

[86] M. Schmittfull, M. Simonović, V. Assassi, and M. Zaldarriaga, Modeling biased tracers at the field level, Phys. Rev. D **100**, 043514 (2019).

[87] J. C. Jackson, Fingers of God: A critique of Rees' theory of primoridal gravitational radiation, Mon. Not. R. Astron. Soc. **156**, 1P (1972).

[88] Z. Vlah and M. White, Exploring redshift-space distortions in large-scale structure, J. Cosmol. Astropart. Phys. 03 (2019) 007.

[89] S.-F. Chen, Z. Vlah, and M. White, Consistent modeling of velocity statistics and redshift-space distortions in one-loop perturbation theory, J. Cosmol. Astropart. Phys. 07 (2020) 062.

[90] M. M. Ivanov, Cosmological constraints from the power spectrum of eBOSS emission line galaxies, Phys. Rev. D **104**, 103514 (2021).

[91] L. Senatore and M. Zaldarriaga, The IR-resummed effective field theory of large scale structures, J. Cosmol. Astropart. Phys. 02 (2015) 013.

[92] T. Baldauf, M. Mirbabayi, M. Simonović, and M. Zaldarriaga, Equivalence principle and the baryon acoustic peak, Phys. Rev. D **92**, 043514 (2015).

[93] D. Blas, M. Garny, M. M. Ivanov, and S. Sibiryakov, Time-sliced perturbation theory for large scale structure I: General formalism, J. Cosmol. Astropart. Phys. 07 (2016) 052.

[94] Z. Vlah, M. White, and A. Aviles, A lagrangian effective field theory, J. Cosmol. Astropart. Phys. 09 (2015) 014.

[95] Z. Vlah, U. Seljak, M. Y. Chu, and Y. Feng, Perturbation theory, effective field theory, and oscillations in the power spectrum, J. Cosmol. Astropart. Phys. 03 (2016) 057.

[96] M. Crocce and R. Scoccimarro, Renormalized cosmological perturbation theory, Phys. Rev. D **73**, 063519 (2006).

[97] M. Crocce and R. Scoccimarro, Nonlinear evolution of baryon acoustic oscillations, Phys. Rev. D **77**, 023533 (2008).

[98] A. Vasudevan, M. M. Ivanov, S. Sibiryakov, and J. Lesgourgues, Time-sliced perturbation theory with primordial non-Gaussianity and effects of large bulk flows on inflationary oscillating features, J. Cosmol. Astropart. Phys. 09 (2019) 037.

[99] Y.-S. Song, A. Taruya, and A. Oka, Cosmology with anisotropic galaxy clustering from the combination of power spectrum and bispectrum, J. Cosmol. Astropart. Phys. 08 (2015) 007.

[100] F. Bernardeau, M. Crocce, and R. Scoccimarro, Constructing regularized cosmic propagators, Phys. Rev. D **85**, 123519 (2012).

[101] E. Sefusatti, M. Crocce, and V. Desjacques, The matter bispectrum in N-body simulations with non-Gaussian initial conditions, Mon. Not. R. Astron. Soc. **406**, 1014 (2010).

[102] R. Mehrem, J. T. Londergan, and M. H. Macfarlane, Analytic expressions for integrals of products of spherical Bessel functions, J. Phys. A **24**, 1435 (1991).

[103] T. Brinckmann and J. Lesgourgues, MontePython 3: Boosted MCMC sampler and other features, Phys. Dark Universe **24**, 100260 (2019).

[104] B. Audren, J. Lesgourgues, K. Benabed, and S. Prunet, Conservative constraints on early cosmology: An illustration of the Monte Python cosmological parameter inference code, J. Cosmol. Astropart. Phys. 02 (2013) 001.

[105] A. Lewis, GetDist: A Python package for analysing Monte Carlo samples, arXiv:1910.13970.

[106] D. Blas, J. Lesgourgues, and T. Tram, The cosmic linear anisotropy solving system (CLASS) II: Approximation schemes, J. Cosmol. Astropart. Phys. 07 (2011) 034.

[107] M. M. Ivanov, Y. Ali-Haïmoud, and J. Lesgourgues, H0 tension or T0 tension?, Phys. Rev. D **102**, 063515 (2020).

[108] M. M. Abidi and T. Baldauf, Cubic halo bias in Eulerian and Lagrangian space, J. Cosmol. Astropart. Phys. 07 (2018) 029.

[109] A. Eggemeier, R. Scoccimarro, M. Crocce, A. Pezzotta, and A. G. Sánchez, Testing one-loop galaxy bias: Power spectrum, Phys. Rev. D **102**, 103530 (2020).

[110] T. Lazeyras, C. Wagner, T. Baldauf, and F. Schmidt, Precision measurement of the local bias of dark matter halos, J. Cosmol. Astropart. Phys. 02 (2016) 018.

[111] T. Lazeyras and F. Schmidt, Beyond LIMD bias: A measurement of the complete set of third-order halo bias parameters, J. Cosmol. Astropart. Phys. 09 (2018) 008.

[112] A. Barreira, T. Lazeyras, and F. Schmidt, Galaxy bias from forward models: Linear and second-order bias of IllustrisTNG galaxies, J. Cosmol. Astropart. Phys. 08 (2021) 029.

[113] S. Pueblas and R. Scoccimarro, Generation of vorticity and velocity dispersion by orbit crossing, Phys. Rev. D **80**, 043504 (2009).

[114] M. Schmittfull, M. Simonović, M. M. Ivanov, O. H. E. Philcox, and M. Zaldarriaga, Modeling galaxies in redshift space at the field level, J. Cosmol. Astropart. Phys. 05 (2021) 059.

[115] R. E. Smith, R. K. Sheth, and R. Scoccimarro, An analytic model for the bispectrum of galaxies in redshift space, Phys. Rev. D **78**, 023523 (2008).

[116] O. H. E. Philcox, M. M. Ivanov, M. Simonović, and M. Zaldarriaga, Combining full-shape and BAO analyses of galaxy power spectra: A 1.6% CMB-independent constraint on H_0, J. Cosmol. Astropart. Phys. 05 (2020) 032.

[117] O. H. E. Philcox, Cosmology without window functions: Quadratic estimators for the galaxy power spectrum, Phys. Rev. D **103**, 103504 (2021).

[118] O. H. E. Philcox, Cosmology without window functions: Cubic estimators for the galaxy bispectrum, Phys. Rev. D **104**, 123529 (2021).

[119] O. H. E. Philcox and M. M. Ivanov, BOSS DR12 full-shape cosmology: ΛCDM constraints from the large-scale galaxy power spectrum and bispectrum monopole, Phys. Rev. D **105**, 043517 (2022).

[120] E. Di Valentino *et al.*, Cosmology intertwined III: $f\sigma_8$ and S_8, Astropart. Phys. **131**, 102604 (2021).

[121] A. Aghamousa *et al.* (DESI Collaboration), The DESI experiment part I: Science, targeting, and survey design, arXiv:1611.00036.

[122] R. Laureijs *et al.* (EUCLID Collaboration), Euclid definition study report, arXiv:1110.3193.

[123] L. Amendola *et al.*, Cosmology and fundamental physics with the Euclid satellite, Living Rev. Relativity **21**, 2 (2018).

[124] A. de Mattia *et al.*, The completed SDSS-IV extended baryon oscillation spectroscopic survey: Measurement of the BAO and growth rate of structure of the emission line galaxy sample from the anisotropic power spectrum between redshift 0.6 and 1.1, Mon. Not. R. Astron. Soc. **501**, 5616 (2021).

[125] D. Wadekar, M. M. Ivanov, and R. Scoccimarro, Cosmological constraints from BOSS with analytic covariance matrices, Phys. Rev. D **102**, 123521 (2020).

[126] N. Kaiser, Clustering in real space and in redshift space, Mon. Not. R. Astron. Soc. **227**, 1 (1987).